OPEN ACCESS



The Regulated NiCu Cycles with the New 57 Cu(p, γ) 58 Zn Reaction Rate and Its Influence on Type I X-Ray Bursts: the GS 1826–24 Clocked Burster

Yi Hua Lam (藍乙華)^{1,2}, Ning Lu (盧寧)^{1,2,3}, Alexander Heger^{4,5,6,7}, Adam Michael Jacobs^{7,8}, Nadezda A. Smirnova⁹, Teresa Kurtukian Nieto⁹, Zac Johnston^{7,8}, and Shigeru Kubono (久保野茂)^{10,11}, Institute of Modern Physics, Chinese Academy of Sciences, Lanzhou 730000, People's Republic of China; lamyihua@impcas.ac.cn

1 Institute of Modern Physics, Chinese Academy of Sciences, Beijing 100049, People's Republic of China; lamyihua@impcas.ac.cn

2 School of Nuclear Science and Technology, Lanzhou University, Lanzhou 730000, People's Republic of China

3 School of Nuclear Science and Technology, Lanzhou University, Lanzhou 730000, People's Republic of China

4 School of Physics and Astronomy, Monash University, Victoria 3800, Australia; alexander.heger@monash.edu

5 OzGrav-Monash—Monash Centre for Astrophysics, School of Physics and Astronomy, Monash University, VIC 3800, Australia

6 Center of Excellence for Astrophysics, Michigan State University, East Lansing, MI 48824, USA

8 Department of Physics and Astronomy, Michigan State University, East Lansing, MI 48824, USA

9 CENBG, CNRS/IN2P3 and University of Bordeaux, Chemin du Solarium, 33175 Gradignan cedex, France

10 RIKEN Nishina Center, 2-1 Hirosawa, Wako, Saitama 351-0198, Japan

11 Center for Nuclear Study, University of Tokyo, 2-1 Hirosawa, Wako, Saitama 351-0198, Japan

12 Center for Nuclear Study, University of Tokyo, 2-1 Hirosawa, Wako, Saitama 351-0198, Japan

13 Center for Nuclear Study, University of Tokyo, 2-1 Hirosawa, Wako, Saitama 351-0198, Japan

14 Center for Nuclear Study, University of Tokyo, 2-1 Hirosawa, Wako, Saitama 351-0198, Japan

15 Center for Nuclear Study, University of Tokyo, 2-1 Hirosawa, Wako, Saitama 351-0198, Japan

Abstract

During the X-ray bursts of GS 1826–24, a "clocked burster", the nuclear reaction flow that surges through the rapid-proton capture process path has to pass through the NiCu cycles before reaching the ZnGa cycles that moderate further hydrogen burning in the region above the germanium and selenium isotopes. The 57 Cu(p, γ) 58 Zn reaction that occurs in the NiCu cycles plays an important role in influencing the burst light curves found by Cyburt et al. We deduce the 57 Cu(p, γ) 58 Zn reaction rate based on the experimentally determined important nuclear structure information, isobaric-multiplet-mass equation, and large-scale shell-model calculations. Based on the isobaric-multiplet-mass equation, we propose a possible order of 1_1^+ - and 2_3^+ -dominant resonance states and constrain the resonance energy of the 1_2^+ state. The latter reduces the contribution of the 1_2^+ -dominant resonance state. The new reaction rate is up to a factor of 4 lower than the Forstner et al. rate recommended by JINA REACLIB v2.2 at the temperature regime sensitive to clocked bursts of GS 1826–24. Using the simulation from the one-dimensional implicit hydrodynamic code KEPLER to model the thermonuclear X-ray bursts of the GS 1826–24 clocked burster, we find that the new 57 Cu(p, γ) 58 Zn reaction rate, coupled with the latest 56 Ni(p, γ) 57 Cu and 55 Ni(p, γ) 56 Cu reaction rates, redistributes the reaction flow in the NiCu cycles and strongly influences the burst ash composition, whereas the 59 Cu(p, α) 56 Ni and 59 Cu(p, α) 56 Zn reactions suppress the influence of the 57 Cu(p, α) 58 Zn reaction and diminish the impact of nuclear reaction flow that bypasses the important 56 Ni waiting point induced by the 55 Ni(p, γ) 56 Cu reaction on the burst light curve.

Unified Astronomy Thesaurus concepts: Nucleosynthesis (1131); Explosive nucleosynthesis (503); Nuclear astrophysics (1129); Neutron stars (1108); Nuclear abundances (1128); X-ray bursts (1814); Computational methods (1965); Nuclear physics (2077)

1. Introduction

Thermonuclear (Type I) X-ray bursts (XRBs) originate in the high-density-temperature degenerate envelope of a neutron star in a close low-mass X-ray binary during thermonuclear runaways (Woosley & Taam 1976; Joss 1977). The envelope consists of stellar material accreted from the low-mass companion star. Every XRB episode encapsulates abundant information on the hydrodynamics and thermal states of the evolution of the degenerate envelope (Woosley et al. 2004), the structure of the accreting neutron star (Steiner et al. 2010), the rapid-proton capture (rp-) process path of synthesized nuclei (Van Wormer et al. 1994; Schatz et al. 1998), and the burst ashes that become compositional inertia for the succeeding bursts before sinking into the neutron-star crust (Keek & Heger 2011; Meisel et al. 2018).

Original content from this work may be used under the terms of the Creative Commons Attribution 4.0 licence. Any further distribution of this work must maintain attribution to the author(s) and the title of the work, journal citation and DOI.

XRBs are driven by the triple- α reaction (Joss 1978), α pprocess (Woosley & Weaver 1984), and rp-process (Wallace & Woosley 1981; Wiescher et al. 1987) and are constrained by β decay and the proton drip line. After breaking out from the hot CNO cycle, the nuclear reaction flows enter the sd-shell nuclei region via αp -processes; this is also the region in which the αp processes are dominant. Then, the reaction flows continue to the pf-shell nuclei region, first going through a few important cycles at the light pf-shell nuclei, e.g., the CaSc cycle, and then reaching the medium pf-shell nuclei where the NiCu and ZnGa cycles reside (Van Wormer et al. 1994). After breaking out from the ZnGa cycles and the GeAs cycle, which may transiently and weakly exist, and passing through Ge and Se isotopes, the reaction flows surge through the heavier proton-rich nuclei where rp-processes actively burn the remaining hydrogen accreted from the companion star; eventually, the reaction flows stop at the SnSbTe cycles (Schatz et al. 2001). This rp-process path is indicated in the pioneering GS 1826-24 clocked burster model (Woosley et al. 2004; Heger et al. 2007).

The 57 Cu(p, γ) 58 Zn reaction that draws material from the 56 Ni waiting point via the 56 Ni(p, γ) 57 Cu branch is located in the

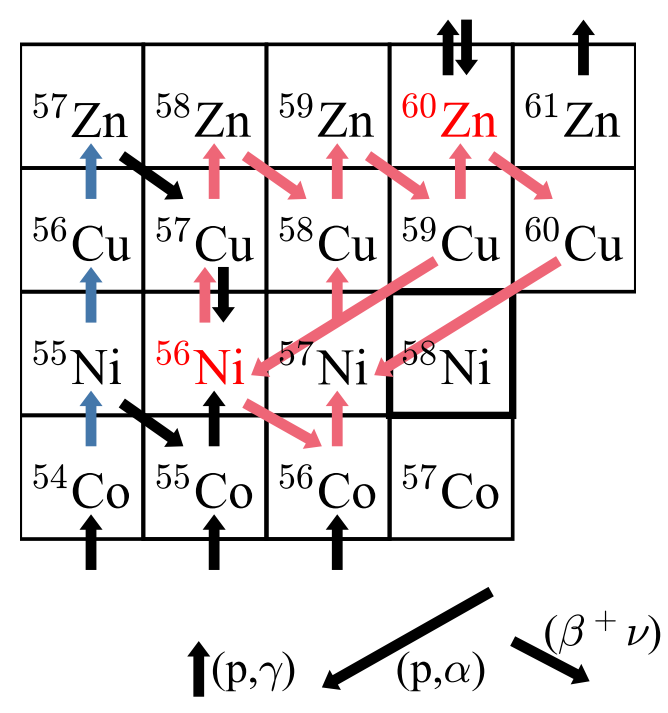


Figure 1. The rp-process path passing through the NiCu cycles. Stable nuclei are represented by thick black squares, and waiting points are shown in red texts. The NiCu cycles are displayed as red arrows. The NiCu 1 cycle consists of $^{56}\text{Ni}(p,\gamma)^{57}\text{Cu}(p,\gamma)^{58}\text{Cu}(p,\gamma)^{58}\text{Cu}(p,\gamma)^{59}\text{Zn}(\beta^+\nu)^{59}\text{Cu}(p,\alpha)^{56}\text{Ni}$ reactions, and the NiCu II cycle is a series of $^{57}\text{Ni}(p,\gamma)^{58}\text{Cu}(p,\gamma)^{59}\text{Zn}(\beta^+\nu)^{59}\text{Cu}(p,\gamma)$ $^{60}\text{Zn}(\beta^+\nu)^{60}\text{Cu}(p,\alpha)^{57}\text{Ni}$ reactions (Van Wormer et al. 1994). The other sub-NiCu II cycle, $^{56}\text{Ni}(\beta^+\nu)^{56}\text{Co}(p,\gamma)^{57}\text{Ni}(p,\gamma)^{58}\text{Cu}(p,\gamma)^{59}\text{Zn}(\beta^+\nu)^{59}\text{Cu}(p,\alpha)^{56}\text{Ni},$ can also be established. The matter flow induced by the $^{55}\text{Ni}(p,\gamma)^{56}\text{Cu}$ reaction to bypass the ^{56}Ni waiting point is illustrated in blue arrows.

NiCu I cycle (Figure 1). The influence of this reaction on the XRB light curve and on burst ash abundances was studied by Cyburt et al. (2016), and they concluded that the 57 Cu(p, γ) 58 Zn reaction is the fifth most influential (p,γ) reaction that affects the light curve of the GS 1826-24 clocked burster (Makino 1988; Tanaka 1989; Ubertini et al. 1999). Forstner et al. (2001) constructed the 57 Cu(p, γ) 58 Zn reaction rate based on shell-model calculations and predicted the properties of important resonances. Later, Langer et al. (2014) experimentally confirmed some low-lying energy levels of 58Zn, which are dominant resonances contributing to the 57 Cu(p, γ) 58 Zn reaction rate at temperature range $0.3 \lesssim T(GK) \lesssim 2.0$. With the high-precision measurement of these energy levels, Langer et al. largely reduced the rate uncertainty by up to three orders of magnitude compared to the Forstner et al. reaction rate. Nevertheless, the order of the 1_1^+ - and 2_3^+ -dominating resonance states was unconfirmed, and the 1⁺₂ resonance state, which is one of the dominant resonances at the XRB temperature range,

 $0.8 \lesssim T(\text{GK}) \lesssim 2$, was not detected in their experiment. The $^{55}\text{Ni}(p,\gamma)^{56}\text{Cu}$ reaction rate was recently determined by Valverde et al. (2019) and Ma et al. (2019) with the highly precisely measured ^{56}Cu mass (Valverde et al. 2018) and the precisely measured excited states of ^{56}Cu (Ong et al. 2017). In fact, Ma et al. (2019) found that the $^{55}\text{Ni}(p,\gamma)^{56}\text{Cu}$ reaction rate was underestimated by up to one order of magnitude by Valverde et al. (2018) due to the incorrect penetrability scaling factor, causing a set of wrongly determined burst ash abundances of nuclei A = 55-60. Figure 2 presents the comparison of the $^{55}\text{Ni}(p,\gamma)^{56}\text{Cu}$ reaction rates deduced by Valverde et al. (2019), Ma et al. (2019), and Fisker et al.

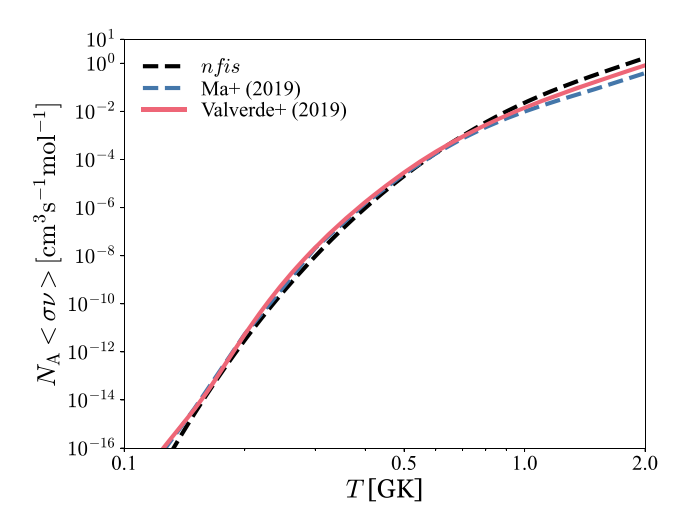


Figure 2. The 55 Ni(p, γ) 56 Cu thermonuclear reaction rates. Valverde et al. (2019) corrected the 55 Ni(p, γ) 56 Cu reaction rate (red solid line) after Ma et al. (2019) proposed a 55 Ni(p, γ) 56 Cu reaction rate (blue dashed line) based on the 56 Cu proton separation energy, S_p (56 Cu) = 579.8 keV and pointed out the incorrect penetrability scaling factor implemented by Valverde et al. (2018). The Fisker et al. (2001) rate (black dashed line) is recommended by JINA REACLIB v2.2 (Cyburt et al. 2010).

(2001). The reaction rate was then corrected by Valverde et al. (2019) and used in their updated one-zone XRB model indicating that the reaction flow bypassing the important 56 Ni waiting point could be established. Based on the updated zero-dimensional one-zone hydrodynamic XRB model, the extent of the impact the newly corrected 55 Ni(p, γ) 56 Cu reaction induces on the bypassing reaction flow, however, causes merely up to 5% difference in the productions of nuclei A = 55-65 (Valverde et al. 2019). Moreover, due to the zero-dimensional feature of the one-zone XRB model, the distribution of synthesized nuclei along the mass coordinate in the accreted envelope is unknown, and importantly, the one-zone hydrodynamic XRB model does not match with any observation.

In the present work, we reanalyze the nuclear structure information and perform simulations with the aim to constrain the reaction flows in the NiCu cycles and to analyze their impact on the clocked bursts of the GS 1824-26 burster. In Section 2, we present the formalism for the reaction rate calculation and introduce the isobaric-multiplet-mass equation (IMME) that we use to cross-check the order of the 1_1^+ and 2_3^+ states in 58 Zn, the dominating resonances for the 57 Cu(p, γ) 58 Zn reaction, and to estimate the energy of the 1^+_2 resonance state. The deduced 57 Cu(p, γ) 58 Zn reaction rate is discussed in detail in Section 3. Using the one-dimensional multizone hydrodynamic KEPLER code (Weaver et al. 1978; Woosley et al. 2004; Heger et al. 2007), we model a set of XRB episodes matched with the GS 1826-24 burster with the newly deduced 57 Cu(p, γ) 58 Zn, Valverde et al. (2019) 55 Ni(p, γ) 56 Cu, and Kahl et al. $(2019)^{56}$ Ni $(p,\gamma)^{57}$ Cu reaction rates. We study the influence of these rates and also investigate the effect of the ⁵⁶Ni-waiting-point bypassing matter flow induced by the 55 Ni(p, γ) 56 Cu reaction. The implication of the new 57 Cu(p, γ) 58 Zn, 55 Ni(p, γ) 56 Cu, and 56 Ni(p, γ) 57 Cu reaction rates on the XRB light curve, the nucleosyntheses in and evolution of the accreted envelope of GS 1826-24 (clocked burster) along the mass coordinate, is presented in Section 4. The conclusion of this work is given in Section 5.

2. Reaction Rate Calculations

The total thermonuclear proton-capture reaction rate is expressed as the sum of resonant- (res) and direct-capture (DC) on the ground state and thermally excited states in the target nucleus, and each capture with given initial and final states is weighted by its individual population factor (Fowler & Hoyle 1964; Rolfs & Rodney 1988),

$$N_{A}\langle \sigma v \rangle = \sum_{i} (N_{A}\langle \sigma v \rangle_{\text{res}}^{i} + N_{A}\langle \sigma v \rangle_{\text{DC}}^{i})$$

$$\times \frac{(2J_{i} + 1)e^{-E_{i}/kT}}{\sum_{n} (2J_{n} + 1)e^{-E_{n}/kT}},$$
(1)

where J are the angular momenta of the initial states of the target nucleus and E are the energies of these initial states.

Resonant rate. The resonant reaction rate for proton capture on a target nucleus in its initial state, i, $N_A \langle \sigma v \rangle_{\rm res}^i$, is a sum over all respective compound nucleus states j above the proton separation energy (Rolfs & Rodney 1988; Iliadis 2007). The resonant rate can be expressed as (Fowler et al. 1967; Schatz et al. 2005)

$$N_{A} \langle \sigma v \rangle_{\text{res}}^{i} = 1.54 \times 10^{11} (\mu T_{9})^{-3/2} \times \sum_{j} \omega \gamma_{ij} \exp\left(-\frac{11.605 E_{\text{res}}^{ij}}{T_{9}}\right), \tag{2}$$

in units of cm³ s⁻¹ mol⁻¹, where the resonance energy in the center-of-mass system, $E_{\rm res}^{ij}=E_{\rm x}^{\ j}-S_{\rm p}-E_i$ (in MeV in Equation (2)), is the energy difference between the compound nucleus $E_{\rm x}^{\ j}$ state and the sum of the excitation energies of the initial state E_i and the respective proton threshold, $S_{\rm p}$. For the capture on the ground state, $E_i=0$. μ is the reduced mass of the entrance channel in atomic mass units ($\mu=A_{\rm T}/(1+A_{\rm T})$, with $A_{\rm T}$ the target mass number), and T_9 is the temperature in gigakelvin (GK). The resonance energy and strength in Equation (2) are given in units of MeV. The resonance strength, $\omega\gamma_{ij}$, taken in MeV in Equation (2), reads

$$\omega \gamma_{ij} = \frac{2J_j + 1}{2(2J_i + 1)} \frac{\Gamma_{p}^{ij} \times \Gamma_{\gamma}^{j}}{\Gamma_{\text{total}}^{j}}, \tag{3}$$

where J_i is the target spin and J_j , Γ_p^{ij} , Γ_γ^j , and Γ_{total}^j are a spin, proton-decay width, γ -decay width, and total width of the compound nucleus state j, respectively. Assuming that other decay channels are closed (Audi et al. 2017) in the considered excitation energy range of the compound nuclei, the total width becomes $\Gamma_{total}^j = \Gamma_\gamma^j + \Gamma_p^{ij}$. Within the shell-model formalism that we use here, the proton width can be expressed as

$$\Gamma_{\rm p} = \sum_{\rm nlj} C^2 S({\rm nlj}) \, \Gamma_{\rm sp}({\rm nlj}), \tag{4}$$

where Γ_{sp} is a single-particle width for the capture of a proton with respect to a given (nlj) quantum orbital in a spherically symmetric mean-field potential, while $C^2S(\text{nlj})$ denotes a corresponding spectroscopic factor containing information of the structure of the initial and final states. The Γ_{sp} can either be estimated from proton-scattering cross sections in a Woods–Saxon potential with the adjusted potential depth to reproduce known proton energies (WSPOT code); ¹² or alternatively, it

can also be obtained from the potential barrier penetrability calculation as (Van Wormer et al. 1994; Herndl et al. 1995)

$$\Gamma_{\rm sp} = \frac{3\hbar^2}{uR^2} P_1(E),\tag{5}$$

where $R = r_0 \times (1 + A_T)^{1/3}$ fm (with $r_0 = 1.25$ fm) is the nuclear channel radius, and the Coulomb barrier penetration factor P_1 is

$$P_1(E) = \frac{kR}{F_1^2(E) + G_1^2(E)},\tag{6}$$

where $k=\sqrt{2\mu E}/\hbar$ and E is the proton energy in the center-of-mass system; F_1 and G_1 are the regular and irregular Coulomb functions, respectively. In the present work, we follow the same procedure as was used by Lam et al. (2016) to get the proton widths of the important $^{57}\text{Cu}(p,\gamma)^{58}\text{Zn}$ resonances up to the Gamow window. The maximum difference between the $\Gamma_{\rm sp}$ described by the two methods above is below 40% for the present work.

Gamma-decay widths are obtained from electromagnetic reduced transition probabilities $B(\Omega L; J_i \rightarrow J_f)$ (Ω stands for electric or magnetic), which contain the nuclear structure information of the resonance states and the final bound states. The corresponding gamma-decay widths for the most contributed transitions (M1 and E2) can be expressed as (Brussaard & Glaudemans 1977)

$$\Gamma_{\text{M1}} = 1.16 \times 10^{-2} E_{\gamma}^{3} B(\text{M1}), \text{ and}$$

$$\Gamma_{\text{E2}} = 8.13 \times 10^{-7} E_{\gamma}^{5} B(\text{E2}), \tag{7}$$

where B(M1) are in μ_N^2 , B(E2) are in $e^2 fm^4$, E_γ are in keV, while Γ_{M1} and Γ_{E2} are in units of eV. The B(M1) values have been obtained from free g factors, i.e., $g_p^s = 5.586$, $g_n^s = -3.826$ and $g_p^l = 1$, $g_n^l = 0$, whereas the B(E2) values have been obtained from standard effective charges, $e_p = 1.5e$ and $e_n = 0.5e$ (Honma et al. 2004). We use experimental energies, E_γ , when available. The total electromagnetic decay width is obtained from the summation of all partial decay widths for a given initial state.

Information on nuclear structure. The essential information needed to estimate the resonant rate contribution of $^{57}\text{Cu}(p,\gamma)^{58}\text{Zn}$ consists of the resonance energies of the compound nucleus $^{57}\text{Cu}+p$, one-proton transfer spectroscopic factors, and proton- and gamma-decay widths. The properties of resonances sensitive to the $^{57}\text{Cu}(p,\gamma)^{58}\text{Zn}$ reaction rate in the XRB temperature range are provided by Langer et al. (2014). Nevertheless, the order of the l_1^+ and 2_3^+ states of ^{58}Zn was undetermined by Langer et al. In order to reproduce the Langer et al. rate, we find that the dominant resonances for the temperature range from 1 to 2 GK sensitive to XRB are not limited to the measured 2_4^+ state. The 1_2^+ and 2_5^+ resonance states, which were not observed by Langer et al., also contribute to the total reaction rate at temperatures $0.8 \leq T(\text{GK}) \leq 2$.

In the present study, we use the IMME to constrain the energies of experimentally unknown, but important resonance state, in 58 Zn, i.e., the order of the l_1^+ and 2_3^+ states of 58 Zn and the energy of the l_2^+ state. A similar method was exploited earlier by Richter et al. (2011) and Richter & Brown (2012, 2013) to provide the missing experimental information

¹² https://people.nscl.msu.edu/~brown/reaction-codes/

of the nuclear level schemes. Also, the same method was used by Schatz & Ong (2017) to estimate the unknown nuclear masses important for the reverse (p,γ) rates. Assuming that the isospin-symmetry-breaking forces are two-body operators of the isovector and isotensor character, the mass excesses of the members of an isobaric multiplet $(I=1,I_z=-I,-I+1,...,I)$ show at most a quadratic dependence on I_z , as expressed by the IMME (Wigner 1957),

$$M_L(\alpha, I) = a(\alpha, I) + b(\alpha, I)I_z + c(\alpha, I)I_z^2, \tag{8}$$

where $M_{I_z}(\alpha, I)$ is the mass excess of a quantum state of isospin (I, I_z) , and $\alpha = (A, J^\pi, N_{\rm exc},...)$ are the nuclear mass number A, excited state number $N_{\rm exc}$, and all other quantum numbers labeling the quantum state. The a, b, and c coefficients reflect contributions from the isoscalar, isovector, and isotensor parts of the effective nucleon–nucleon interaction, respectively (see Ormand & Brown (1989) or Lam et al. (2013a, 2013b) for details). For an isobaric-triplet state $(I=1, I_z=-1, 0, +1)$, we can form from Equation (8) a system of three linear equations and, therefore, express the IMME c coefficient in terms of three mass excesses as

$$c = [M_{-1}(\alpha, 1) + M_{+1}(\alpha, 1) - 2M_0(\alpha, 1)]/2.$$
 (9)

In turn, if we know the mass excesses of the $I_z = 0$ and $I_z = 1$ isobaric-multiplet members and a theoretical c coefficient, the mass excess of a proton-rich member ($I_z = -1$) can be found via a simple relation:

$$M_{-1}(\alpha, 1) = 2M_0(\alpha, 1) - M_{+1}(\alpha, 1) + 2c(\alpha, 1).$$
 (10)

This equation defines the method that we use in the present paper.

We first obtain a set of theoretical IMME c coefficients for the lowest and excited A = 58 triplets, including those that involve the dominant resonances. To this end, we perform large-scale shell-model calculations in the full pf shell-model space using the NUSHELLX@MSU shell-model code (Brown & Rae 2014) with the charge-dependent Hamiltonian, which is constructed from the modern isospin-conserving Hamiltonian (GXPF1a; Honma et al. 2004, 2005), the two-body Coulomb interaction, strong charge-symmetry-breaking and chargeindependence-breaking terms (Ormand & Brown 1989), and the pf shell-model space isovector single-particle energies (Ormand & Brown 1995). The Hamiltonian is referred to as "cdGX1A" and was used by Smirnova et al. (2016, 2017) to investigate the isospin mixing in the β -delayed proton emission of pf-shell nuclei. The IMME c coefficients of these dominant resonances permit us to determine the order of the 1_1^+ and 2_3^+ states of ⁵⁸Zn and to estimate the resonance energy of the 1⁺₂ resonance state. Properties of all other resonances situated within the Gamow window corresponding to the XRB temperature range are computed using the KSHELL code (Shimizu et al. 2019) in a full pf shell-model space with the GXPF1a Hamiltonian. For A = 57 and 58, Hamiltonian matrices of dimensions up to 1.58×10^9 have been diagonalized using the thick-restart block Lanczos method.

The theoretical IMME *c* coefficients are then compared with the available experimental data compiled in Lam et al. (2013b) and updated in the present work by the recently reevaluated mass excesses of ⁵⁸Zn, ⁵⁸Cu, and ⁵⁸Ni (Audi et al. 2017; AME2016). For excited multiplets, the experimental information on level schemes have been taken from Langer et al. (2014) for ⁵⁸Zn;

Table 1 Experimental Isospin I=1 States in 58 Zn, 58 Cu, and 58 Ni Organized in Isobaric Multiplets and the Corresponding Experimental and Theoretical IMME c Coefficients

J_i^{π}		$E_{\rm x}~({\rm keV})^{\rm a,b}$	IMME c (keV)		
J_i	⁵⁸ Zn	⁵⁸ Cu	⁵⁸ Ni	Exp.b	Theo.c
0_1^+	0	203	0	200 (25)	235 (22)
2_{1}^{+}	1356 (3)	1653	1454	156 (25)	179 (22)
4_{1}^{+}	2499 (4)	2750	2459	133 (25)	154 (22)
2_{2}^{+}	2609 (6)	2931	2775	166 (25)	162 (22)
$1_{l}^{+\mathbf{d}}$	2861 (4)	~3100-~3200	2902		133 (22)
2_3^{+d}	2904 (5)		3038		192 (22)
2_{4}^{+}	3265 (6)	3513	3264	156 (25)	143 (22)
3_{1}^{+}	3378 (5)		3421		141 (22)
1_{2}^{+}		~3900-~4100	3594		142 (22)
2_{5}^{+}			3898		161 (22)

Notes. Tentative spin and parity assignments are proposed on the basis of the IMME theory for the states (bold texts) without firm experimental assignments. ^a Only uncertainties of (or more than) 1 keV based on the evaluation of Nesaraja et al. (2010) are shown.

from Rudolph & McGrath (1973), Rudolph et al. (1998), Rudolph et al. (2000) for 58 Cu; and from Jongsma et al. (1972), Honkanen et al. (1981), Johansson et al. (2009), and Rudolph et al. (2002) for 58 Ni. The uncertainty of the measured 58 Zn mass (Seth et al. 1986) dominates the experimental IMME c coefficient uncertainties and propagates to the proton separation energy of 58 Zn, $S_p(^{58}$ Zn) = 2.280 ± 0.050 MeV (AME2016). In general, theoretical c coefficients are seen to be in robust agreement with the respective experimental values. The comparison yields the rms deviation of about 22 keV, which we assign to the calculated values as the theoretical uncertainty; see Table 1.

According to the recent compilation of IMME c coefficients of isobaric multiplets with A = 6-58 (Lam et al. 2013b), the IMME c coefficients exhibit a gradually decreasing trend as a function of A with values ranging between about 400 and 150 keV. As is well known from the data, the c coefficients of triplets show a prominent staggering effect, being split into two families: the values of c coefficients inherent to isobars with A = 4n + 2 appear to be systematically higher than those for their A = 4n neighbors, with n being a positive integer. These average values decrease with increasing A approximately as $A^{-1/3}$ as suggested by a uniformly charged liquid drop model. It has also been noticed that the amplitude of staggering decreases with increasing excitation energy manifesting the weakening of the pairing effects in higher excited states (Lam et al. 2013a). In the present study, we extend the compilation of Lam et al. (2013b) and tentatively propose excited isobaric multiplets in the A = 58 triplet. Although the dependence of ccoefficients on excitation energy is less known, from theoretical studies in the sd-shell nuclei, the amplitude of staggering in

b Presently compiled from the evaluated nuclear masses (AME2016) and experimentally measured levels (Jongsma et al. 1972; Rudolph & McGrath 1973; Honkanen et al. 1981; Rudolph et al. 1998, 2000, 2002; Johansson et al. 2009; Langer et al. 2014) according to the procedure implemented by Lam et al. (2013b).

^c Presently calculated with the cdGX1A Hamiltonian based on the full pf shell-model space. The 1_1^+ , 2_3^+ , 3_1^+ , 1_2^+ , and 2_5^+ triplets are not taken into the comparison yielding the rms.

^d An alternative order of the l_1^+ and 2_3^+ states according to IMME dominance to the previous order proposed by Langer et al. (2014).

J_i^π	$E_{\rm x}$ (keV)	Partial Electromagnetic Widths, Γ_{γ} (MeV)			
u _l	* (* ' /	$J_i^\pi o 0_{ m g.s.}^+$	$J_i^\pi o 2_1^+$		
2_{3}^{+}	2861	2.18	3.12		
l_l^+	2904	0.34	7.5		
11+	2861	0.33	7.0		
2_{3}^{+}	2904	2.35	3.38		
	$E_{\rm x}~({\rm keV})$	Electromagnetic decay intensities, I_{γ} (%) $J_{i}^{\pi} \rightarrow 0_{\rm g.s.}^{+}$ $J_{i}^{\pi} \rightarrow 2_{\rm l}^{+}$			
Exp.	2861	7 (2)	8 (2)		
Exp.	2904	3 (1)	13 (2)		

isobaric triplets is expected to gradually diminish in the pf-shell nuclei. Recently, more precise nuclear mass measurements confirmed the persistence of these trends in the pf-shell nuclei (Zhang et al. 2018; Surbrook et al. 2019; Fu et al. 2020). We find that the values of the c coefficients provide a very stringent test for isobaric multiplets as we will see below.

The order of the 1_1^+ and 2_3^+ states. As was mentioned before, the order of the 1_1^+ and 2_3^+ states stays undetermined in the work by Langer et al. (2014) with two plausible energies, 2861 keV and 2904 keV. The character of the electromagnetic decay of those states weakly supports the assignment proposed in that work, that the lower state is a 2_3^+ state and the higher one is the 1_1^+ , I=1 state. Indeed, we can get the ratio of the partial electromagnetic widths for the decay of these states to $0_{g.s.}^+$ and 2_1^+ to be more in reasonable agreement with that assignment as seen from Table 2.

Alternatively, a certain constraint can also be imposed by the IMME. Although the 1_1^+ and 2_3^+ , I=1 states of 58 Cu are not assigned (Nesaraja et al. 2010), from the existing data we find that the best candidate for 2_3^+ could be a state at 3230 ± 20 keV as measured by Rudolph & McGrath (1973) via the (3 He,t) reaction on the 58 Ni target. Taking into account the 2_3^+ (3037.86 \pm 0.16 keV) state of 58 Ni (Nesaraja et al. 2010), we check for resulting values of the corresponding c coefficients for the two states of question in 58 Zn. Thus, we obtain $c=145\pm32$ keV, assuming that the 2_3^+ state in 58 Zn is at 2904 keV, or $c=124\pm32$ keV, assuming that it is at 2861 keV. The former value is closer to the theoretical c coefficient of 192 ±22 keV (Table 1). Based on this indication, we suggest here that the 2904 keV state could be tentatively assigned as 2_3^+ .

For the I_1^+ , I=1 state in ⁵⁸Cu, only an interval of energies can be proposed. Indeed, no low-lying 1^+ , I=1 states have been observed by Fujita et al. (2002, 2007). To understand this fact, we have calculated a Gamow–Teller (GT) strength distribution from the ⁵⁸Ni ground state to the 1^+ states in ⁵⁸Cu using the GXPF1a Hamiltonian. The results are summarized in Table 3. First, we remark that there is a relatively good agreement with the data found in Fujita et al. (2002, 2007). For example, the B(GT) values of 1^+ , I=0 at low energies are comparable. In particular, we also find strong transitions populating the two lowest states. Moreover, our calculation reproduces a relatively large strength fragment at 3.4 MeV, which may be split between two states in the experiment. Second, it can be noticed that the two lowest 1^+ , I=1 states carry a very small amount of the GT strength,

Table 3 Theoretical Gamow–Teller Strength, B(GT), Populating the 1^+ States in 58 Cu Deduced from the cdGX1A Hamiltonian

Isospin, I	$E_{\rm x}~({\rm MeV})$	Gamow–Teller Strengths, $B(GT)^{a}$
0	0.000	0.221
0	1.135	0.190
0	2.181	0.013
0	2.782	0.024
1	3.298	0.001
0	3.353	0.002
0	3.426	0.217
0	3.550	0.000
1	3.612	0.020
0	3.767	0.015
0	3.860	0.076
0	4.321	0.005
0	4.565	0.051
0	4.871	0.151
0	5.035	0.081
0	5.130	0.010
0	5.260	0.023
0	5.358	0.028
0	5.491	0.003
0	5.528	0.000

Note

similar to what Fujita et al. (2007) found also using the KB3G Hamiltonian (Poves et al. 2001). It is therefore well probable that those states either were not observed by charge-exchange experiments or correspond to low statistic counts at around $3.1-3.2 \, \text{MeV}$ in Figure 5 of Fujita et al. (2007). With the tentative assignment of 2_3^+ of ${}^{58}\text{Zn}$ above, we propose an alternative assignment as compared to the work of Langer et al. (2014) and hence the 2861 keV state could be proposed to be 1_1^+ .

The energies of the 1^+_2 and 2^+_5 states. The predicted B(GT) intensity to this state from theory could, in principle, have been seen in the data of the charge-exchange experiment performed by Fujita et al. (2007). Three possible candidates have been reported between 3.6 and 4 MeV as can be seen from Figures 5 and 7 of that article. Taking any of them and using the theoretically predicted IMME c coefficient of the $(A = 58, 1^+_2, I = 1)$ triplet, 142 ± 22 keV, we estimate that the energy of the 58 Zn, 1^+_2 state cannot be below about 3664 ± 22 keV. The uncertainty is based on the comparison presented in Table 1. This IMME-estimated 1^+_2 state is 309 ± 22 keV higher than the one estimated by using GXPF1a Hamiltonian that was used by Langer et al. (2014) to obtain the contribution from the 1^+_2 resonance state for the 57 Cu(p, γ) 58 Zn reaction rate.

resonance state for the 57 Cu(p, γ) 58 Zn reaction rate. There is no best candidate 2_5^+ isobaric analog state in 58 Cu to estimate the 2_5^+ state of 58 Zn. The GXPF1a Hamiltonian predicts the 2_5^+ state to be at 3605 keV excitation energy, and we adopt this value as a lower limit for 58 Zn, being aware that in the mirror nucleus, 58 Ni, its analog is found at 3.898 MeV. Applying the theoretical IMME c coefficient of $(A = 58, 2_5^+, I = 1)$ triplet, 161 ± 22 keV, we can expect that the 2_5^+ , I = 1 state in 58 Cu to be in the energy interval of 3.9–4.1 MeV. Future high-precision experiments measuring the level schemes of 58 Cu and 58 Zn in this energy region may provide more

^a The theoretical *B*(GT) is quenched with the standard quenching factor of 0.77 (Horoi et al. 2007).

information of the $l_1^+,\, l_2^+,\,$ and 2_5^+ isobaric analog states, and the l_2^+ and 2_5^+ states of $^{58}Zn.$

Properties of resonances—With the information on nuclear structure described above, we deduce a set of resonance properties of 58 Zn to construct the new 57 Cu(p, γ) 58 Zn resonant reaction rate within the typical XRB temperature range, e.g., the GS 1826–24 burster. We only consider proton capture on the $3/2_{\rm g.s.}^-$ ground state (g.s.) of 57 Cu as the contribution from proton resonant captures on thermally excited states of 57 Cu are negligible due to rather high-lying excited states. Hence, it is adequate to just present the newly deduced resonance properties of the 57 Cu(p, γ) 58 Zn reaction rate up to the 3_7^+ state (5.250 MeV) in Table 4 within the Gamow window corresponding to the XRB temperature range.

By comparing the $\Gamma_{\gamma}^{2_{3}^{-}}$ produced from the full pf-model space used in the present work with the $\Gamma_{\gamma}^{2_{3}^{+}}$ generated from the four-particle-four-hole truncated scheme used in Langer et al. (2014) calculation, we notice that the present $\Gamma_{\gamma}^{2_{3}^{+}}$ of ⁵⁸Zn (Table 4) is one order of magnitude lower than the one calculated by Langer et al. (2014). Nevertheless, the respective Γ_{p} is two orders of magnitude lower than $\Gamma_{\gamma}^{2_{3}^{+}}$ and, thus, such difference in the $\Gamma_{\gamma}^{2_{3}^{+}}$ state does not impact the respective ω_{γ} .

We note that the inverse assignment of the I_1^+ and 2_3^+ states compared to the Langer et al. (2014) assignment, in fact, changes the contributions of the I_1^+ and 2_3^+ resonance states. This is mainly because the main contributions for the 2_3^+ and 1_1^+ states are the $p_{1/2}$ and $f_{5/2}$ particle captures, respectively. For higher values of the orbital angular momentum 1 of the captured proton, the corresponding width becomes more sensitive to the proton energy because barrier penetrability varies faster. Once the 1^+ state, governed by the f capture, is assigned at a lower excitation energy, its contribution to the resonant rate becomes drastically reduced.

Direct-capture rate—Comparing the direct-capture rate deduced by Fisker et al. (2001) (or by Forstner et al. 2001) with the presently deduced resonant capture rate, we notice that the contribution of direct capture is exponentially lower than the contribution of the dominating resonances throughout XRB related temperature range from 0.3 to 2 GK. Hence, the contribution of the direct-capture rate is negligible for the 57 Cu(p, γ) 58 Zn reaction rate; see Figure 3 which only presents the Fisker et al. direct-capture rate.

3. New 57 Cu(p, γ) 58 Zn Reaction Rate

Table 5 shows the calculated total reaction rate of 57 Cu(p, γ) 58 Zn as a function of temperature. The present (*Present*, hereafter) thermonuclear rate is parameterized in the format proposed by Rauscher & Thielemann (2000) with the expression below,

$$N_{A}\langle \sigma v \rangle = \sum_{i} \exp\left(a_{0}^{i} + \frac{a_{1}^{i}}{T_{9}} + \frac{a_{2}^{i}}{T_{9}^{1/3}} + a_{3}^{i} T_{9}^{1/3} + a_{4}^{i} T_{9} + a_{5}^{i} T_{9}^{5/3} + a_{6}^{i} \ln T_{9}\right).$$

$$(11)$$

These parameters, i.e., a_0 , a_1 , a_2 , a_3 , a_4 , a_5 , and a_6 , are listed in Table 6. The running index i is up to 6 for the *Present* rate for the temperature region, 0.1-2 GK. The parameterized *Present* rate is evaluated according to an accuracy quantity proposed by

Rauscher & Thielemann (2000),

$$\zeta = \frac{1}{n} \sum_{m=1}^{n} \left(\frac{r_m - f_m}{f_m} \right)^2,$$

where n is the number of data points, r_m are the original *Present* rate calculated for each respective temperature, and f_m are the fitted rate at that temperature. With n = 297, ζ is 4.45×10^{-3} , and the fitting error is 5.90% for the temperature range from 0.01 to 3 GK. The parameterized rate is obtained with aid from the Computational Infrastructure for Nuclear Astrophysics (CINA). For rates above 3 GK, one may refer to statistical model calculations to match with the *Present* rate, which is only valid within the mentioned temperature range and fitting errors, see NACRE (Angulo et al. 1999).

We reproduce the Langer et al. rate (Langer et al. 2014), taking into account contributions from the 1_2^+ , 2_4^+ , and 2_5^+ resonance states, which are dominant at temperature region $0.8 \lesssim T(GK) \lesssim 2$; see the top panel in Figure 3. Other contributing resonances to the Langer et al. rate for temperature $T \lesssim 0.8$ GK are also included in Figure 3. The *Present* rate and the respective main contributing resonances with updated Γ_p and Γ_γ widths based on a full *pf*-model space are plotted in the bottom panel of Figure 3. We find that with the new energy of the 1_2^+ state, estimated from the IMME formalism, the contribution of this resonance to the total rate reduces and becomes even less dominant than the contribution of the 2_4^+ resonance state at temperature regime $0.8 \lesssim T(GK) \lesssim 2$.

The comparison of the *Present* rate with the Langer et al. rate and with other reaction rates compiled into JINA REACLIB v2.2 by Cyburt et al. (2010) is shown in Figure 4. The Hauser–Feshbach statistical model rates, i.e., $rath^{14}$, $thra^{15}$, and $ths8^{16}$ are very close to one another from 0.1 to 2.0 GK, and they are lower than the *Present* rate up to an order of magnitude at temperature $T \lesssim 0.9$ GK. Due to the reduction of the contribution from the 1_2^+ resonance state, the *Present* rate is up to a factor of 2 lower than the Langer et al. rate from 0.8 to 2 GK covering the typical maximum temperature of the GS 1826–24 burster, and up to a factor of 4 lower than the *wien2* rate (Forstner et al. 2001) recommended by JINA REACLIB v2.2; see the comparison in the respective ratio in the bottom panel of Figure 4.

By taking into account the uncertainty of $S_p(^{58}Zn)$, we estimate and list the uncertainty of Present $^{57}Cu(p,\gamma)^{58}Zn$ reaction rate as upper and lower limits in Table 5. Both upper and lower limits are shown by the red zone in Figure 4, whereas the uncertainty of the Langer et al. rate is indicated by the blue zone. Even if the uncertainty due to the order of the I_1^+ and I_2^+ states would have been removed, the uncertainty of I_2^+ states would have been removed, the uncertainty of I_2^+ states would have been removed, the uncertainty of I_2^+ states would have been removed, the uncertainty of I_2^+ states would have been removed, the uncertainty of I_2^+ states would have been removed, the uncertainty of I_2^+ states would have been removed, the uncertainty is I_2^+ states would have been removed, the uncertainty is specifically I_2^+ states would have been removed that this is the first I_2^+ reaction rate constructed from important experimental information supplemented with the full I_2^+ shell space shell-model calculation that yields converged resonance energies, I_2^+ and spectroscopic factors; the uncertainty is

http://nucastrodata.org/infrastructure.html

¹⁴ Produced by Rauscher & Thielemann (2000) using the NON-SMOKER code with FRDM mass input (Möller et al. 1995).

¹⁵ Produced by Rauscher & Thielemann (2000) using the NON-SMOKER code with ETFSI-Q mass input (Pearson et al. 1996).

¹⁶ Produced by T. Rauscher using the NON-SMOKER code as part of JINA REACLIB since the v1.0 release (Cyburt et al. 2010).

Table 4 Properties of 58 Zn for the Ground-state Proton Capture in the Present 57 Cu(p, γ) 58 Zn Resonant Rate Calculation

$\overline{J_i^\pi}$	$E_{\rm x}~({\rm MeV})^{\rm a}$	$E_{\rm res}~({ m MeV})^{ m d}$	$C^2S_{7/2}$	$C^2S_{3/2}$	$C^2S_{5/2}$	$C^2S_{1/2}$	Γ_{γ} (eV)	$\Gamma_{\rm p}~({\rm eV})$	$\omega\gamma$ (eV)
			(l=3)	(l=1)	(l=3)	(l = 1)			
0_{1}^{+}	0.000			1.1001					
2_{1}^{+}	1.356 ^b		0.0351	0.8381	0.1459	0.0913	6.736×10^{-4}		
4_{1}^{+}	2.499 ^b	0.219	0.0123		0.6737		1.741×10^{-4}	1.002×10^{-17}	1.127×10^{-17}
2_{2}^{+}	2.609 ^b	0.329 ^e	0.0027	0.5776	0.0063	0.1144	9.034×10^{-3}	1.695×10^{-10}	1.059×10^{-10}
1_{1}^{+}	2.861 ^b	0.581 ^e		0.0000	0.6522	0.0867	7.300×10^{-3}	4.662×10^{-6}	1.747×10^{-6}
2_{3}^{+}	2.904 ^b	0.624 ^e	0.0020	0.0131	0.0103	0.1649	5.278×10^{-3}	3.380×10^{-5}	2.099×10^{-5}
0_{2}^{+}	2.995	0.715		0.4393			4.758×10^{-5}	1.097×10^{-3}	5.700×10^{-6}
4_{2}^{+}	3.263	0.983	0.0016		0.0048		3.589×10^{-4}	1.074×10^{-5}	1.173×10^{-5}
2_{4}^{+}	3.265 ^b	0.985 ^e	0.0005	0.1174	0.4953	0.0002	4.131×10^{-3}	4.338×10^{-2}	2.357×10^{-3}
0_{3}^{+}	3.349	1.069		0.0419			8.758×10^{-4}	4.827×10^{-2}	1.075×10^{-4}
3_{1}^{+}	3.378 ^b	1.098	0.0016	0.0000	0.6849		3.466×10^{-3}	4.649×10^{-3}	1.737×10^{-3}
2_{5}^{+}	3.605	1.325	0.0012	0.0011	0.0302	0.2498	1.387×10^{-2}	3.677	8.637×10^{-3}
1_{2}^{+}	3.664 ^c	1.384 ^e		0.0000	0.1011	0.5980	4.526×10^{-2}	$1.527 \times 10^{+1}$	1.692×10^{-2}
3_{2}^{+}	3.670	1.390	0.0042	0.0000	0.0033		3.680×10^{-4}	1.745×10^{-3}	2.659×10^{-4}
4_{3}^{+}	3.969	1.689	0.0169		0.0077		1.275×10^{-2}	6.250×10^{-2}	1.191×10^{-2}
5_{1}^{+}	4.009	1.729	0.0012				5.162×10^{-4}	4.589×10^{-3}	6.380×10^{-4}
2_{6}^{+}	4.077	1.797	0.0000	0.0019	0.0030	0.0671	2.016×10^{-3}	$3.024 \times 10^{+1}$	1.260×10^{-3}
3_{3}^{+}	4.168	1.888	0.0192	0.0020	0.0312		1.202×10^{-2}	2.044	1.046×10^{-2}
4_{4}^{+}	4.188	1.908	0.0079		0.0087		1.430×10^{-3}	1.468×10^{-1}	1.593×10^{-3}
0_{4}^{+}	4.242	1.962		0.0000			8.661×10^{-3}	0.000	0.000
4_{5}^{+}	4.268	1.988	0.0034		0.0584		1.323×10^{-2}	6.240×10^{-1}	1.458×10^{-2}
2_{7}^{+}	4.270	1.990	0.0035	0.0007	0.0357	0.0001	3.740×10^{-3}	1.477	2.332×10^{-3}
0_{5}^{+}	4.363	2.083		0.0198			1.606×10^{-2}	$4.158 \times 10^{+1}$	2.007×10^{-3}
4_{6}^{+}	4.520	2.240	0.0051		0.0000		6.485×10^{-3}	3.290×10^{-1}	7.154×10^{-3}
3_{4}^{+}	4.546	2.266	0.0003	0.0000	0.0016		3.161×10^{-2}	7.852×10^{-2}	1.972×10^{-2}
5_{2}^{+}	4.594	2.314	0.0065				7.146×10^{-3}	5.545×10^{-1}	9.701×10^{-3}
35+	4.653	2.373	0.0003	0.0000	0.0000		1.428×10^{-2}	3.279×10^{-2}	8.705×10^{-3}
2_{8}^{+}	4.708	2.428	0.0092	0.0000	0.0323	0.0059	2.609×10^{-2}	$4.483 \times 10^{+1}$	1.630×10^{-2}
4_{7}^{+}	4.832	2.552	0.0050		0.0050		1.378×10^{-2}	1.715	1.538×10^{-2}
5_{3}^{+}	4.909	2.629	0.0001				1.751×10^{-3}	2.902×10^{-2}	2.271×10^{-3}
4_{8}^{+}	4.964	2.684	0.0000		0.0090		2.452×10^{-3}	1.692	2.755×10^{-3}
2_{9}^{+}	5.013	2.733	0.0002	0.0027	0.0002	0.0022	3.656×10^{-3}	$9.118 \times 10^{+1}$	2.285×10^{-3}
36+	5.040	2.760	0.0060	0.0000	0.0006		1.759×10^{-2}	2.944	1.530×10^{-2}
49+	5.184	2.904	0.0073		0.0037		2.096×10^{-2}	6.858	2.351×10^{-2}
54+	5.208	2.928	0.0001				7.299×10^{-3}	7.758×10^{-2}	9.173×10^{-3}
2_{10}^{+}	5.227	2.947	0.0001	0.0327	0.0016	0.0023	2.958×10^{-2}	$1.230 \times 10^{+3}$	1.849×10^{-2}
3+	5.250	2.970	0.0001	0.0008	0.0002		1.045×10^{-2}	$2.904 \times 10^{+1}$	9.142×10^{-3}

Notes.

clearly identified, whereas the Hauser–Feshbach statistical model rates may include unknown systematic errors because of their limited capability in estimating level densities of nuclei near to the proton drip line.

4. Implication for Multizone X-Ray Burst Models

We explore the influence of the Present $^{57}Cu(p,\gamma)^{58}Zn$ reaction rate in characterizing the XRB light curves of the GS 1826-24 X-ray source (Makino 1988; Tanaka 1989) and burst ash composition after an episode of XRBs based on one-dimensional multizone hydrodynamic XRB models. The theoretical XRB models matched with the GS 1826-24

clocked burster (Ubertini et al. 1999) are instantiated by the KEPLER code (Weaver et al. 1978; Woosley et al. 2004; Heger et al. 2007) and were used by Heger et al. (2007) to perform the first quantitative comparison with the observed GS 1826–24 light curve. Later, the GS 1826–24 XRB models were used by Cyburt et al. (2016) and by Jacobs et al. (2018) to study the sensitivity of (α, γ) , (α, p) , (p, γ) , and (p, α) nuclear reactions. The GS 1826–24 XRB models are continuously updated and were recently used by Goodwin et al. (2019) and by Johnston et al. (2020) to study the high-density properties of accreted envelopes of the GS 1826–24 clocked burster. The XRB models are fully self-consistent, which take into account the

^a The energy levels of ⁵⁸Zn obtained from the present full *pf*-model space shell-model calculation with the GXPF1a Hamiltonian, except when otherwise quoted from experiment or predicted from IMME.

^b The experimentally determined energy levels of ⁵⁸Zn (Langer et al. 2014).

 $^{^{\}rm c}$ The theoretical energy levels of $^{\rm 58}{\rm Zn}$ predicted from IMME, see text.

^d Calculated by $E_{\rm res} = E_{\rm x} - S_{\rm p} - E_i$ with $S_{\rm p}(^{58}{\rm Zn}) = 2.280 \pm 0.050$ MeV deduced from AME2016 (Audi et al. 2017).

^e Resonances dominantly contributing to the total rate within temperature region of 0.1-2 GK.

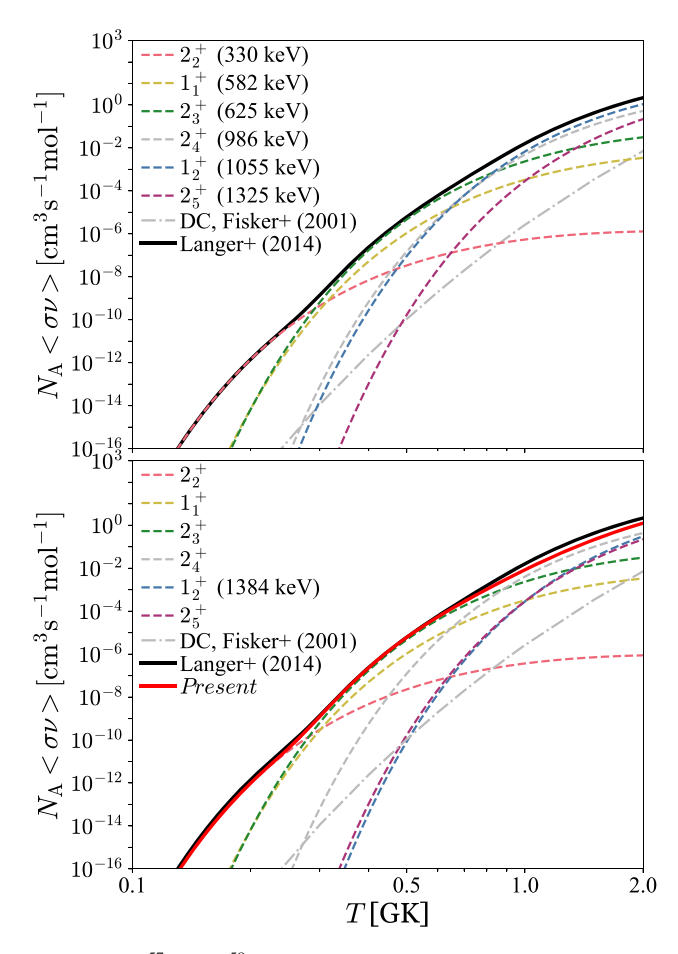


Figure 3. The 57 Cu(p, γ) 58 Zn thermonuclear reaction rates. Top panel: The main contributing resonances of proton captures on the $3/2^-_{g.s.}$ state of 57 Cu in the temperature region of XRB interest are indicated as dashed color lines with the respective resonance energies. Bottom panel: The updated main contributing resonances with the full pf shell-model space calculation for the Γ_{γ} widths and spectroscopic factors, and with the resonance energy of the 1^+_2 state using IMME formalism. See details in the text and Table 4.

$\overline{T_9}$	Centroid (cm ³ s ⁻¹ mol ⁻¹)	Lower Limit (cm ³ s ⁻¹ mol ⁻¹)	Upper Limit (cm ³ s ⁻¹ mol ⁻¹)
0.1	1.44×10^{-20}	1.28×10^{-21}	6.62×10^{-20}
0.2	9.72×10^{-13}	2.39×10^{-13}	1.62×10^{-12}
0.3	1.23×10^{-9}	6.53×10^{-10}	2.78×10^{-9}
0.4	2.34×10^{-7}	2.19×10^{-7}	2.93×10^{-7}
0.5	6.08×10^{-6}	4.23×10^{-6}	9.30×10^{-6}
0.6	5.45×10^{-5}	3.08×10^{-5}	9.90×10^{-5}
0.7	2.80×10^{-4}	1.40×10^{-4}	5.60×10^{-4}
0.8	1.05×10^{-3}	5.08×10^{-4}	2.16×10^{-3}
0.9	3.22×10^{-3}	1.61×10^{-3}	6.43×10^{-3}
1.0	8.42×10^{-3}	4.50×10^{-3}	1.60×10^{-2}
1.1	1.94×10^{-2}	1.11×10^{-2}	3.46×10^{-2}
1.2	3.99×10^{-2}	2.43×10^{-2}	6.72×10^{-2}
1.3	7.51×10^{-2}	4.81×10^{-2}	1.20×10^{-1}
1.4	1.31×10^{-1}	8.73×10^{-2}	2.00×10^{-1}
1.5	2.13×10^{-1}	1.48×10^{-1}	3.14×10^{-1}
1.6	3.30×10^{-1}	2.35×10^{-1}	4.70×10^{-1}
1.7	4.86×10^{-1}	3.56×10^{-1}	6.76×10^{-1}
1.8	6.89×10^{-1}	5.15×10^{-1}	9.36×10^{-1}
1.9	9.44×10^{-1}	7.19×10^{-1}	1.26
2.0	1.26	9.71×10^{-1}	1.65

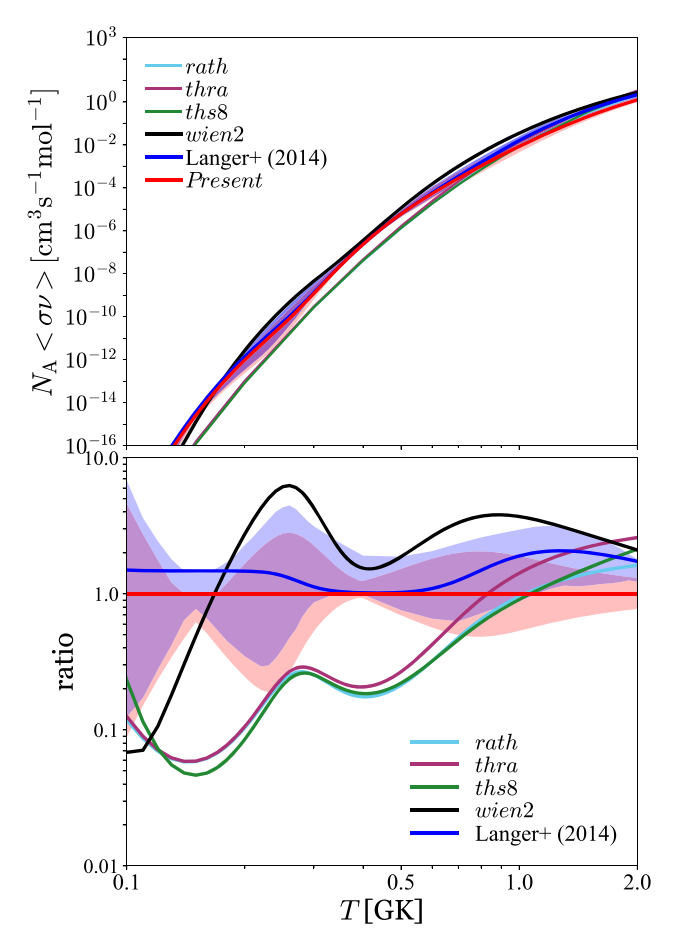


Figure 4. Comparison of $^{57}\text{Cu}(p,\gamma)^{58}\text{Zn}$ thermonuclear reaction rates. Top panel: the *rath*, *thra*, *ths8*, and *wien2* rates are the available rates compiled by Cyburt et al. (2010) and *wien2* is the recommended rate published as part of the JINA REACLIB v2.2 release. All available rates in JINA REACLIB v2.2 define $S_p(^{58}\text{Zn}) = 2.277$ MeV. Bottom panel: the comparison of the *Present* rate with the Langer et al. (2014) rate and with the reaction rates compiled in the JINA REACLIB v2.2. The uncertainties of Langer et al. and the present rates are indicated by the blue and red zones, respectively.

correspondence between the evolution in astrophysical conditions and the feedback of nuclear energy generation in substrates of the accreted envelope. Throughout an episode of outbursts, which may consist of a series of bursts with either an almost consistent or progressively increasing recurrence time, the models are capable to keep updating the evolution of chemical inertia and thermal configurations that drive the nucleosynthesis in the accreted envelope of an accreting neutron star.

The XRB models simulate a grid of Lagrangian zones (Weaver et al. 1978; Woosley et al. 2004; Heger et al. 2007), and each zone independently contains its own isotopic composition and thermal properties. We implement the time-dependent mixing length theory (Heger et al. 2000) to describe the convection transferring heat and nuclei between these Lagrangian zones. KEPLER uses an adaptive thermonuclear reaction network that automatically includes or discards the respective reactions out of the more than 6000 isotopes provided by JINA REACLIB v2.2 (Cyburt et al. 2010).

We adopt the XRB model from Jacobs et al. (2018) to compare with the observed burst light curves of the GS 1826–24 clocked burster. The model had been used by Jacobs et al. (2018)

Table 6Parameters of the 57 Cu(p, γ) 58 Zn Centroid Reaction Rate

i	a_0	a_1	a_2	a_3	a_4	a_5	a_6
1	$-2.70569 \times 10^{+1}$	$-2.54150 \times 10^{+0}$	-4.59592×10^{-4}	4.46992×10^{-3}	-5.27022×10^{-4}	2.68353×10^{-5}	-1.50113
2	$-1.09645 \times 10^{+1}$	$-3.81827 \times 10^{+0}$	1.79997×10^{-2}	-4.00723×10^{-2}	5.02873×10^{-3}	-4.19260×10^{-4}	-1.48386
3	$1.45160 \times 10^{+0}$	$-7.25300 \times 10^{+0}$	-1.15250×10^{-2}	4.54761×10^{-2}	-3.78671×10^{-3}	4.62772×10^{-4}	-1.45082
4	$6.17102 \times 10^{+0}$	$-1.15201 \times 10^{+1}$	-1.08160×10^{-2}	1.93951×10^{-1}	-1.02466×10^{-3}	3.29115×10^{-2}	-1.54743
5	$7.93110 \times 10^{+0}$	$-1.62517 \times 10^{+1}$	1.03977×10^{-1}	-6.19113×10^{-2}	4.30871×10^{-2}	-5.16600×10^{-4}	-1.45643
6	$7.11511 \times 10^{+0}$	$-1.54875 \times 10^{+1}$	5.54672×10^{-2}	-1.08431×10^{-2}	1.08004×10^{-2}	-7.96518×10^{-4}	-1.41275

in a recent sensitivity study of nuclear reactions. To match the modeled light curve with the observed light curve and recurrence time, $\Delta t_{\rm rec} = 5.14 \pm 0.7$ hr, of Epoch Jun 1998 of the GS 1826 −24 burster, we adjust the accreted ¹H, ⁴He, and CNO metallicity fractions to 0.71, 0.2825, and 0.0075, respectively. The accretion rate is tuned to a factor of 0.122 of the Eddington-limited accretion rate, $M_{\rm Edd}$. This adjusted XRB model with the associated nuclear reaction library (JINA REACLIB v2.2) characterizes the baseline model in this work. Note that the wien2 rate is the recommended 57 Cu(p, γ) 58 Zn reaction rate in JINA REACLIB v2.2. Other XRB models that adopt the same astrophysical configurations but implement the Present astrophysical configurations but implement the *Present* 57 Cu(p, γ) 58 Zn; or the corrected 55 Ni(p, γ) 56 Cu (Valverde et al. 2019); or the *Present* 57 Cu(p, γ) 58 Zn and Valverde et al. corrected 55 Ni(p, γ) 56 Cu; or Langer et al. 57 Cu(p, γ) 58 Zn, Valverde et al. corrected 55 Ni(p, γ) 56 Cu, and Kahl et al. (2019) 56 Ni(p, γ) 57 Cu; or the *Present* 57 Cu(p, γ) 58 Zn, Valverde et al. corrected 55 Ni(p, γ) 56 Cu, and Kahl et al. 56 Ni(p, γ) 57 Cu reaction rates are denoted as the $Present^{\dagger}$, $Present^{\dagger}$, $Present^{\Diamond}$, and $Present^{\S}$ models, respectively. The $Present^{\heartsuit}$ and $Present^{\S}$ models implement a factor of 0.120 of $\dot{M}_{\rm Edd}$ for the accretion rate in order to obtain a modeled recurrence time close to the observation, proposing that either the *Present* or Langer et al. 57 Cu(p, γ) 58 Zn reaction rate, which is lower than the wien2 rate, shortens the recurrence time by up to 5%.

We then simulate a series of 40 consecutive XRBs for the baseline, $Present^{\dagger}$, $Present^{\ddagger}$, $Present^{\spadesuit}$, $Present^{\heartsuit}$, and $Present^{\S}$ models; and only the last 30 bursts are summed up with respect to the time resolution and then averaged to yield a burst lightcurve profile. The first 10 bursts simulated from each model are excluded because these bursts undergo a transition from a chemically fresh envelope with unstable burning to an enriched envelope with chemically burned-in burst ashes and stable burning. Throughout the transition, the enriched burst ashes are recycled in the succeeding burst heating, which gradually stabilizes the following bursts. The averaging procedure applied on the modeled light curves is similar to the method performed by Galloway et al. (2017) to produce an averaged light-curve profile from the observed data set of Epoch Jun 1998. The epoch was recorded by the Rossi X-ray Timing Explorer (RXTE) Proportional Counter Array (Galloway et al. 2004, 2008, 2020) and were compiled into the Multi-Instrument Burst Archive¹⁷ by Galloway et al. (2020).

The burst luminosity, L_x , obtained from each model is transformed and related to the observed flux, F_x , via the relation (Johnston et al. 2020)

$$F_{\rm x} = \frac{L_{\rm x}}{4\pi d^2 \xi_{\rm b} (1+z)^2},\tag{12}$$

where d is the distance; ξ_b takes into account of the possible deviation of the observed flux from an isotropic burster luminosity due to the scattering and blocking of the emitted electromagnetic wave by the accretion disk (Fujimoto 1988; He & Keek 2016), and the redshift, z, rescales the light curve when transforming into an observer's frame. d and $\xi_{\rm b}$ are combined to form the modified distance $d\sqrt{\xi_{\mathrm{b}}}$ by assuming that the anisotropy factors of the burst and persistent emissions are degenerate with distance. We include the entire burst time span of an averaged observational data to fit our modeled burst light curves of each model to the observed light curve. The best-fit $d\sqrt{\xi_h}$ and (1+z) factors of the baseline, Present[†], Present[‡], $Present^{\spadesuit}$, $Present^{\heartsuit}$, and $Present^{\S}$ modeled light curves to the averaged-observed light curve and the recurrence time of Epoch June 1998 are 7.28 kpc and 1.29, 7.32 kpc and 1.29, 7.32 kpc and 1.29, 7.32 kpc and 1.28, 7.30 kpc and 1.29, and 7.62 kpc and 1.29, respectively. Using these redshift factors, we obtain a set of modeled recurrence times that are close to the observation. The recurrence times of baseline, Present † , $Present^{\ddagger}$, $Present^{\spadesuit}$, $Present^{\heartsuit}$, and $Present^{\S}$ are 4.85, 4.91, 4.91, 4.88, 4.96, and 4.95 hr, respectively. Though further reducing the accretion rate for each model improves the matching between modeled and observed recurrence time, all modeled burst light curves remain similar. For instance, the recurrence time of the *Present*§ model $\Delta t_{\rm rec} = 4.95$ hr is produced with a defining accretion rate as 0.120 $\dot{M}_{\rm Edd}$, and the produced burst light curve is similar to other modeled light curves in the present work.

The top panel of Figure 5 illustrates the comparison between the best-fit modeled and observed XRB light curves. The evolution time of the light curve is relative to the burst-peak time, t=0 s. The overall averaged flux deviations between the observed epoch and each of these theoretical models, *baseline*, $Present^{\dagger}$, $Present^{\dagger}$, $Present^{\odot}$, and $Present^{\S}$, in units of $10^{-9} {\rm erg~cm}^{-2} {\rm s}^{-1}$, are 1.154, 1.170, 1.172, 1.133, 1.181, and 1.147, respectively. The deviations between the $Present^{\S}$ (and $Present^{\S}$) and observed light curve throughout the whole time span of the observed light curve are displayed in the bottom panel of Figure 5.

The observed burst peak is thought to be located in the time regime t = -2.5 to 2.5 s (top-left inset in Figure 5), and at the vicinity of the modeled light-curve peaks of *baseline*, $Present^{\dagger}$, $Present^{\dagger}$, $Present^{\dagger}$, $Present^{\dagger}$, and $Present^{\dagger}$. The modeled light curves of baseline, $Present^{\dagger}$, $Present^{\dagger}$, $Present^{\dagger}$, $Present^{\dagger}$, and $Present^{\dagger}$ at the near-burst-peak region t = -4.5 to 5.5 s are almost indiscernible.

All modeled light curves are less enhanced than the observed light curve at t = 8-80 s, and the decrement is even augmented around t = 13 and 40 s, increasing the deviation between the

¹⁷ https://burst.sci.monash.edu/minbar/

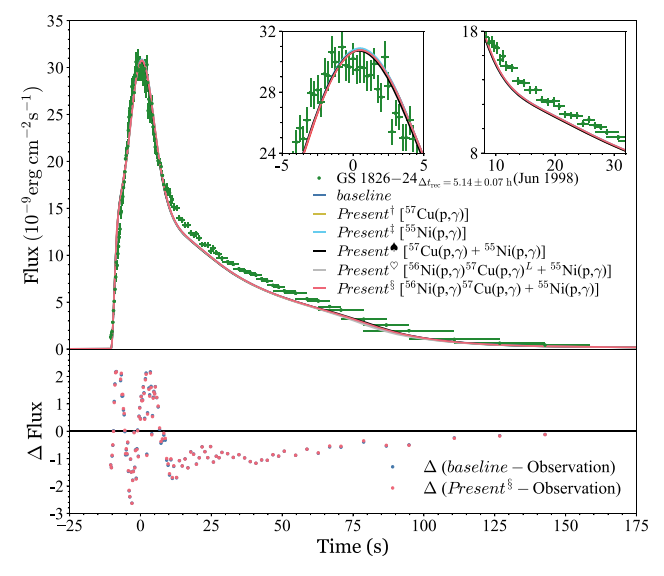


Figure 5. The light curves of the GS 1826–24 clocked burster as a function of time. Top panel: the best-fit *baseline*, $Present^{\dagger}$, $Present^{\dagger}$, $Present^{\dagger}$, and $Present^{\dagger}$ modeled light curves compared to the observed light curve and recurrence time of Epoch June 1998. Both insets in the top panel magnify the light-curve portions at t=-5 to 5 s (left inset) and at t=8-32 s (right inset). Bottom panel: the deviation between the best-fit *baseline* (or *Present*[§]) modeled light curves and the observed light curve.

modeled and observed light curves (bottom panel in Figure 5). From the time regime at $t=78\,\mathrm{s}$ onward until the burst-tail end, all modeled burst light curves are enhanced. Overall, all modeled light-curve profiles are similar and note that the observed burst tail is reproduced from $t=78\,\mathrm{s}$ onward until the burst-tail end.

To investigate the microphysics behind the difference between both modeled burst light curves of the *baseline* and *Present*§ models, we consider the 39th, the 42nd, and the 41st bursts for the *baseline*, *Present* $^{\circ}$, and *Present* $^{\circ}$ models, respectively. These bursts resemble the respective averaged light-curve profile presented in Figure 5. The reference time of the accreted envelope and nucleosynthesis in the following discussion is also relative to the burst-peak time, t=0 s.

The moment before and during the onset. After the preceding burst, the synthesized proton-rich nuclei in the accreted envelope go through β^+ decays and enrich the region around stable nuclei with long half-lives, e.g., 60 Ni, 64 Zn, 68 Ge, and ⁷⁸Se, which are the remnants of waiting points. When the accreted envelope evolves to the moment just before the onset of the succeeding XRB, due to the continuing nuclear reactions that occur in unburned hydrogen above the base of the accreted envelope, the temperature of the envelope increases up to a maximum value of about 0.93 GK at the moment $t = -10 \,\mathrm{s}$ for the baseline, Present[♥], and Present[§] scenarios; see Figure 6. At the moment just before the onset, some nuclei have already been synthesized and stored in the NiCu cycles, i.e., the NiCu I and II cycles (Van Wormer et al. 1994), and the sub-NiCu II cycle (Figure 1), see the top-left and bottom-right insets of the top-left, bottom-left, and top-right panels of Figure 6. Among the isotopes in the NiCu cycles, the highly synthesized nuclei having mass fractions of more than 2×10^{-4} are 59 Zn, 58 Zn, 57 Zn, 58 Ni, 59 Cu, 58 Cu, 57 Cu, and 60 Cu isotopes, and the 56 Ni and 60 Zn waiting points, whereas the ⁵⁶Co and ⁶⁰Cu isotopes having analogous mass-fraction distributions in the envelope are converted to ⁵⁷Ni and ⁶¹Zn,

respectively (the lower-right insets in the top-left, bottom-left, and top-right panels of Figure 6).

We find that although the reaction flow induced by the ⁵⁵Ni(p, γ)⁵⁶Cu(p, γ)⁵⁷Zn branch noticeably bypasses the ⁵⁶Ni waiting point and enriches ⁵⁷Zn for the *baseline*, *Present* $^{\circ}$, and Present[§] scenarios, it eventually has to go through the 57 Zn($\beta^+\nu$) 57 Cu(p, γ) 58 Zn branch and combines with the NiCu cycles and then breaks out from the NiCu cycles to the ZnGa cycles; see the upper-left insets in the top-left, bottom-left, and top-right panels of Figure 6. Due to the rather weak 57 Zn(p, γ) 58 Ga reaction, the 55 Ni(p, γ) 56 Cu(p, γ) 57 Zn reactions and the subsequent 57 Zn($\beta^+\nu$) 57 Cu(p, γ) 58 Zn branch redirect an appreciable amount of material away from the ⁵⁶Ni waiting point, but the redirecting branch does not store material. Moreover, the newly corrected 55 Ni(p, γ) 56 Cu reaction rate is lower than the one recommended in JINA REACLIB v2.2 (Figure 2), causing less enrichment of 57 Zn in the $Present^{\heartsuit}$ and Present[§] scenarios (bottom-right panel of Figure 6). This explains why neither the newly corrected nor the recommended 55 Ni(p, γ) 56 Cu reaction rate exhibiting significant influence on the light curve of the GS 1826-24 burster and abundances of synthesized heavier nuclei. Also, the corrected 55 Ni(p, γ) 56 Cu reaction rate is not as influential as claimed by Valverde et al. (2018, 2019). Note that the one-zone models used by Valverde et al. (2018, 2019) do not reproduce any burst light curves that are matched with observations. We remark that the baseline model that uses the recommended 55 Ni(p, γ) 56 Cu reaction rate in JINA REACLIB v2.2 has already manifested the possibility of the bypassing reaction flow of the ⁵⁶Ni waiting point without replacing the recommended rate by Valverde et al. (2019) corrected rate because the recommended 55 Ni(p, γ) 56 Cu reaction rate is stronger than the Valverde et al. corrected reaction rate; see Figure 2.

At this moment, more than 60% of mass zones in the accreted envelope, where nuclei heavier than CNO isotopes are densely synthesized, has temperature above 0.8 GK. The *Present* $^{57}\text{Cu}(p,\gamma)^{58}\text{Zn}$ reaction rate is up to a factor of 2 lower than the Langer et al. rate from 0.8 to 2 GK due to the reduction of the domination of the 1⁺₂ resonance state (bottom panel of Figure 4), reducing the transmutation rate of ⁵⁷Cu to ⁵⁸Zn. This situation impedes the 56 Ni(p, γ) 57 Cu(p, γ) 58 Zn reaction flow while enhancing the reaction flow bypassing the important ⁵⁶Ni waiting point, causing a higher production of ⁵⁵Ni in the Present[§] scenario (bottom-right panel of Figure 6). Meanwhile, Valverde et al. corrected 55 Ni(p, γ) 56 Cu reaction rate implemented in the *Present*§ scenario reduces the production of ⁵⁷Zn and induces the reaction flow to ⁵⁷Cu. These reaction flows are regulated with new reaction rates and then produce a rather similar ⁵⁸Zn abundance in the *baseline* and *Present*[§] scenarios that are about a factor of 1.2 higher than the ⁵⁸Zn abundance in the $Present^{\heartsuit}$.

Note that the productions of 55 Ni, 56 Cu, 57 Zn, 56 Ni, 57 Cu, and 58 Zn based on the $Present^{\circ}$ and $Present^{\$}$ are discernible due to the correlated influence among the Present (or Langer et al. 2014) 57 Cu(p, γ) 58 Zn, Valverde et al. (2019) corrected 55 Ni(p, γ) 56 Cu, and Kahl et al. (2019) 56 Ni(p, γ) 57 Cu reaction rates. The continuous impact from the correlated influence among these reactions and 59 Cu(p, α) 56 Ni that cycles the reaction flow back to the reaction series in the NiCu cycles since the onset subsequently influences the burst ash composition at the burst-tail end.

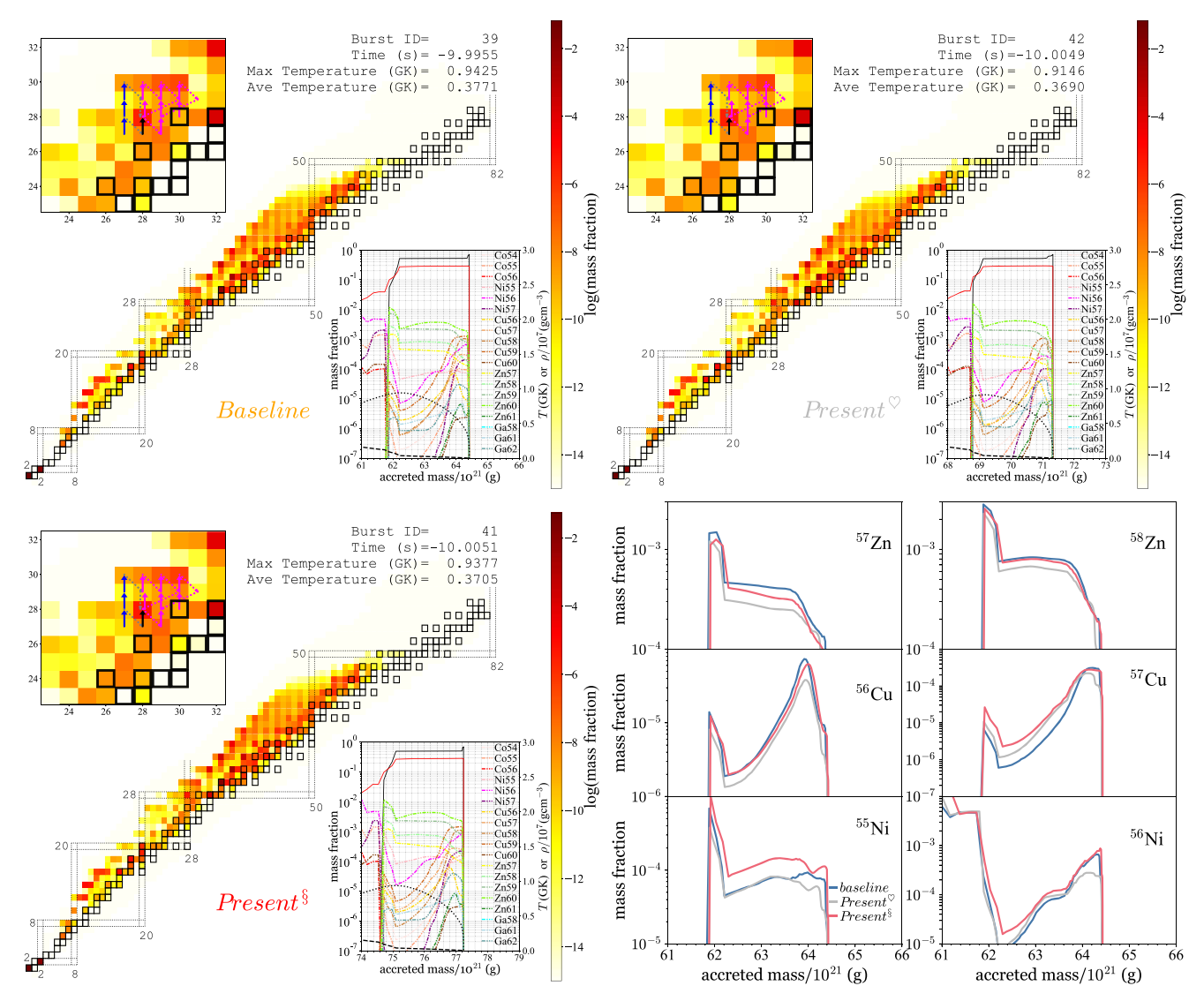


Figure 6. The nucleosynthesis and evolution of envelope corresponds to the moment just before the onset of the 39th burst for *baseline* (top-left panel), of the 42nd for *Present* $^{\circ}$ (top-right panel), and of the 41st burst for *Present* $^{\circ}$ (bottom-left panel) scenarios. The averaged abundances of synthesized nuclei are represented by color tones referring to the right color scale in the nuclear chart of each panel. The black squares are stable nuclei. The top-left insets in each panel magnify the regions related to the NiCu and ZnGa cycles. Upward-pointing arrows indicate the (p, γ) reactions, whereas downward-pointing arrows show the photodisintegration (γ, p) reactions. Slanting arrows from left to right depict $(\beta^+\nu)$ decays and long slanting arrows from right to left represent (p,α) reactions. These arrows are merely used to guide the eyes. The bottom-right insets in each panel present the corresponding temperature (black dotted line) and density (black dashed line) of each mass zone, referring to the right y-axis, and the abundances of synthesized nuclei, referring to the left y-axis, in the accreted envelope regime where nuclei heavier than CNO isotopes are densely synthesized. The abundances of H and He are represented by black and red solid lines, respectively. Bottom-right panel: The comparisons of abundances of 55 Ni, 56 Cu, 57 Zn, 56 Ni, 57 Cu, and 58 Zn of *baseline*, *Present* $^{\circ}$, and *Present* $^{\circ}$ at the respective time snapshot. These abundances are plotted with respect to the mass coordinate of the *baseline* accreted envelope regime.

The mass fraction of 57 Cu in the *baseline* is lower than the one in the $Present^{\heartsuit}$ and $Present^{\S}$ scenarios because the newly updated 56 Ni(p, γ) 57 Cu by Kahl et al. (2019) implemented in $Present^{\heartsuit}$ and $Present^{\S}$ is about up to a factor of 9 higher than the recommended 56 Ni(p, γ) 57 Cu rate from JINA REACLIB v2.2 used in *baseline* at a temperature region of around 1 GK. Nevertheless, the mass fraction of 58 Zn in the *baseline* is about a factor of 1.2 higher than the one in the $Present^{\S}$ scenario. This reflects a stronger flow of 57 Cu(p, γ) 58 Zn in the *baseline* than in the $Present^{\S}$ scenario. Such stronger flow is because the recommended wien2 57 Cu(p, γ) 58 Zn reaction rate from JINA REACLIB v2.2 used in $Present^{\S}$ about up to a factor of 4 higher than the $Present^{\S}$ Cu(p, γ) 58 Zn reaction rates at the temperature region around 1 GK. Meanwhile, the induced 57 Zn($\beta^+\nu$) 57 Cu flow from the reaction flow bypassing the

important ⁵⁶Ni waiting point stacks up the abundance of ⁵⁷Cu in the $Present^{\$}$ scenario. Hence, a strong flow of the ⁵⁶Ni(p, γ)⁵⁷Cu coupled with a weak flow of the ⁵⁷Cu(p, γ)⁵⁸Zn in the $Present^{\$}$ scenario and the stacked-up ⁵⁷Cu eventually yield a set of almost similar mass fractions of ⁵⁸Zn along the mass zones in the accreted envelope during the onset for both *baseline* and $Present^{\$}$ scenarios. On the other hand, synthesized nuclei heavier than ⁶⁸Se for the *baseline* is almost as extensive as the $Present^{\$}$ scenario; see the nuclear chart in Figure 6. This indicates the reaction flow is regulated at the ⁶⁰Zn waiting point by the ⁵⁹Cu(p, α)⁵⁶Ni reaction that competes with the ⁵⁹Cu(p, γ)⁶⁰Zn reaction. Furthermore, after the reaction flow breaks out from the NiCu cycles through the ⁵⁹Cu(p, γ)⁶⁰Zn(p, γ)⁶¹Ga branch to the ZnGa cycles (Van Wormer et al. 1994), it is stored in the ZnGa cycles before

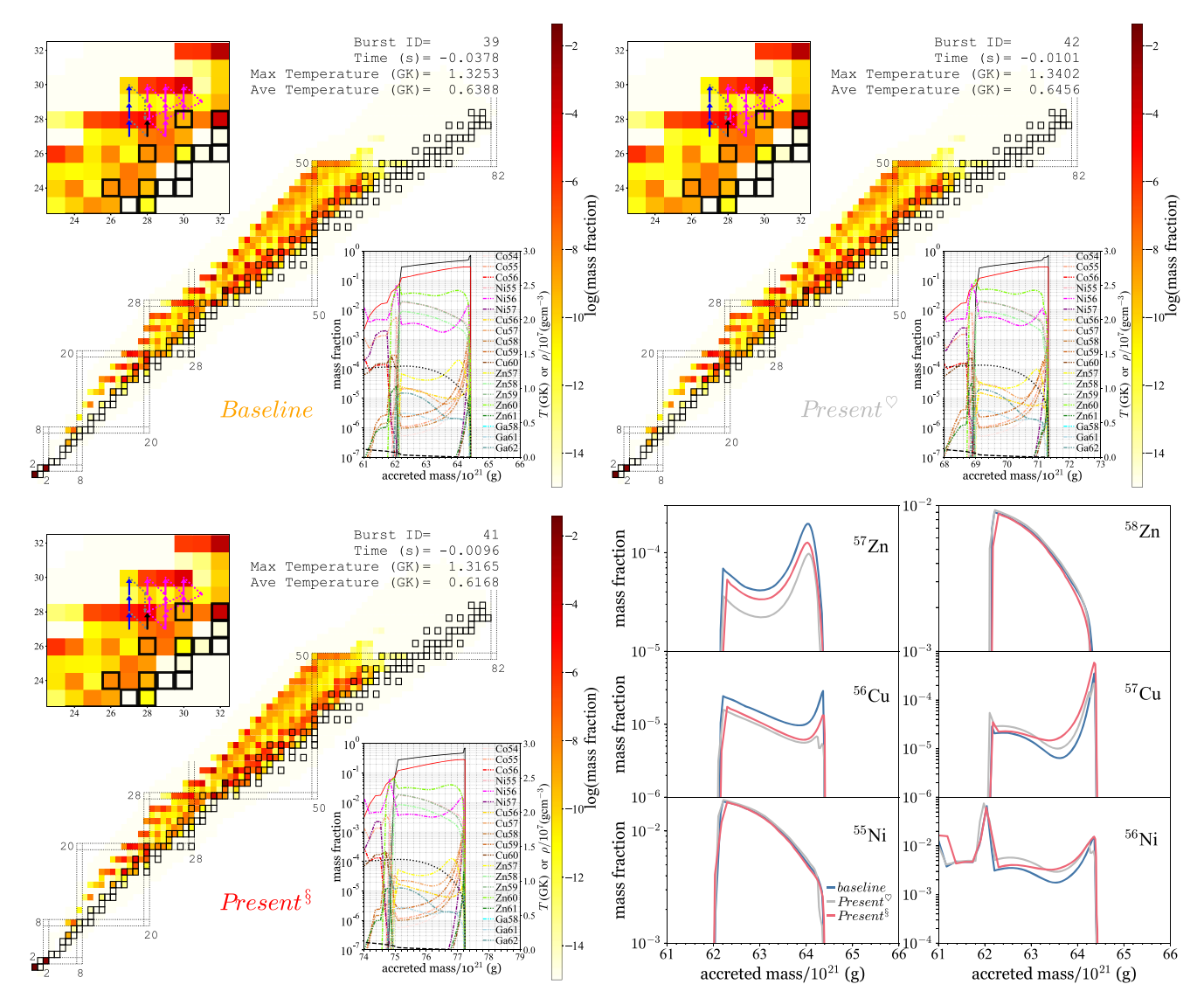


Figure 7. The nucleosynthesis and evolution of envelope corresponds to the moment at the immediate vicinity of the burst peak for *baseline* (top-left panel), *Present* (top-right panel), and *Present* (bottom-left panel) scenarios. See Figure 6 for further description.

surging through nuclei heavier than ⁶⁸Se. We find that the GeAs cycle that involves the two-proton sequential capture of ⁶⁴Ge consisting of ⁶⁴Ge(p, γ) ⁶⁵As(p, γ) ⁶⁶Se reactions could weakly exist in the middle of onset until the moment after burst peak (Lam et al. 2022); see the nucleosynthesis charts in Figures 6, 7, and 8. A new ⁶⁵As(p, γ) ⁶⁶Se reaction rate based on a more precise ⁶⁶Se mass is desired to constrain the transient period, nonetheless, the fact that the transient existence of the weak GeAs cycle is not ruled out for the GS 1826–24 burster.

The ZnGa cycles were recently investigated by Y. H. Lam et al. (2022, in preparation) using the same GS 1826-24 clocked burster model as is used in this work and the full *pf*-model space shell-model calculation. They found that the GeAs cycle that follows the ZnGa cycles only weakly exists for a brief period, which could last until t = 21.4-58.6 s after the burst peak (Lam et al. 2022). This causes some reactions relevant to the ZnGa cycles to become decisive in controlling the reaction flow reaching nuclei heavier than the Ge and Se isotopes where extensive H-burning via (p,γ) reactions occur. These influential reactions are 59 Cu (p,γ) and 61 Ga (p,γ) , which were identified and marked by Cyburt et al. (2016) as the top

four most sensitive reactions on clocked burst light curve. Y. H. Lam et al. (2022, in preparation) found that the 59 Cu(p, γ) and 61 Ga(p, γ) reactions characterize the burst light curve of the GS 1826–24 clocked burster at $t \approx 8$ –30 s after the burst peak and the burst-tail end. Preliminary results of the investigation of the ZnGa cycles were presented in the supplemental material of Hu et al. (2021) prior to Y. H. Lam et al. (2022, in preparation).

We notice that the balance between the 56 Ni(p, γ) 57 Cu and 57 Cu(p, γ) 58 Zn reactions also redistributes the reaction flow to the NiCu II cycle and then the reaction flow eventually joins with the NiCu I cycle and branches out to the ZnGa cycles at the 60 Zn waiting point or follows the 60 Cu(p, γ) 61 Zn(p, γ) 62 Ga reactions branches out to the ZnGa II cycle. Then, the joint reaction flow surges through the proton-rich region heavier than 64 Ge where (p, γ) reactions actively burn hydrogen and intensify the rise of burst light curve from t=-10 s up to t=0 s (burst peak).

The moment at the immediate vicinity of the burst peak. As the redistributing and reassembling of reaction flow from the moment of onset until the burst peak regulate a rather similar feature of abundances in the NiCu cycles (the lower-right insets

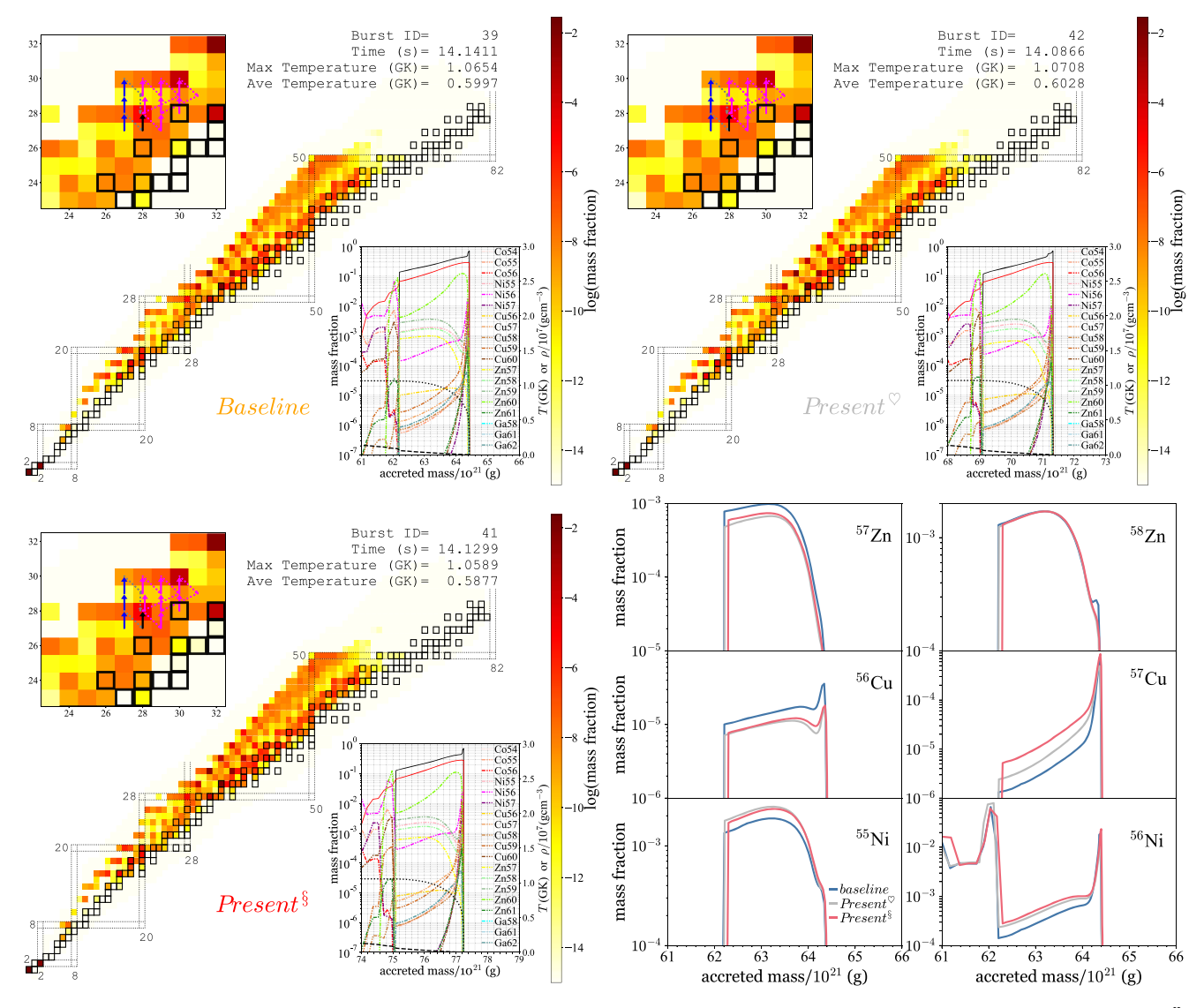


Figure 8. The nucleosynthesis and evolution of envelope corresponds to the moment of around 14 s after the burst peak for *baseline* (top-left panel), *Present*[©] (top-right panel), and *Present*[§] (bottom-left panel) scenarios. See Figure 6 for further description.

in the top-left, bottom-left, and top-right panels of Figure 7), the maximum envelope temperatures of the *baseline*, $Present^{\circ}$, and $Present^{\S}$ scenarios are rather similar. These outcomes cause burst peaks of the *baseline*, $Present^{\S}$, and $Present^{\S}$ scenarios to be almost close to each other; see the left inset in the upper panel of Figure 5 and the maximum envelope temperatures in Figure 7.

The moment after the burst peak. At $t \approx 14\,\mathrm{s}$ and $T \approx 1.06\,\mathrm{GK}$ (maximum envelope temperature), the redistribution of reaction flow since the moment of onset mentioned above slightly keeps the reaction flow in NiCu cycles for somehow longer time and slightly delays the reaction flow from passing through the waiting point $^{60}\mathrm{Zn}$ in the $Present^\$$ scenario. The small delay allows the reaction flow to leak out from the NiCu cycles at a later time and to burn hydrogen along the way, reaching isotopes heavier than $^{68}\mathrm{Se}$ via (p,γ) reactions, and this situation mildly deviates the burst light curve of $Present^\$$ from the light curves of $Present^\$$ from the light curves of $Present^\$$

The moment at the burst-tail end. The observed burst-tail end of Epoch June 1998 of the GS 1826–24 burster is closely reproduced by the baseline, Present[⋄], and Present[⋄] models,

meaning that the H burning in these models recesses accordingly to produce a set modeled light curves in good agreement with observation. At $t=85\,\mathrm{s}$, the light curves of baseline and $Present^{\circ}$ deviate from the light curve of $Present^{\$}$ by about $0.3\times10^{-9}\mathrm{erg}~\mathrm{cm}^{-2}\mathrm{s}^{-1}$. Based on the analysis of the influence of the $^{57}\mathrm{Cu}(p,\gamma)^{58}\mathrm{Zn}$ reaction rate, we anticipate that if the actual energies of the 1_2^+ and 2_5^+ resonance states are even higher than the presently estimated ones using the IMME formalism, the contributions of these two resonance states to the total rate are exponentially reduced, and the 2_4^+ resonance state becomes the only dominant resonance at $T=1-2\,\mathrm{GK}$ for the $^{57}\mathrm{Cu}(p,\gamma)^{58}\mathrm{Zn}$ reaction rate, and thus the modeled burst light curve is more diminished at the burst peak and at $t=8-32\,\mathrm{s}$, whereas at $t=65-150\,\mathrm{s}$, the $Present^{\$}$ light curve is more enhanced compared to the $Present^{\$}$

From $t \approx 14$ s onward until $t \approx 180$ s, the regulation of the NiCu cycles gradually deviates for the production of ⁵⁸Zn due to the accumulated effect from the correlated influence among the latest ⁵⁶Ni(p, γ)⁵⁷Cu, ⁵⁷Cu(p, γ)⁵⁸Zn, and ⁵⁵Ni(p, γ)⁵⁶Cu reaction rates, despite the suppression induced by the ⁵⁹Cu(p, α)⁵⁶Ni reaction; see the bottom-right panel in

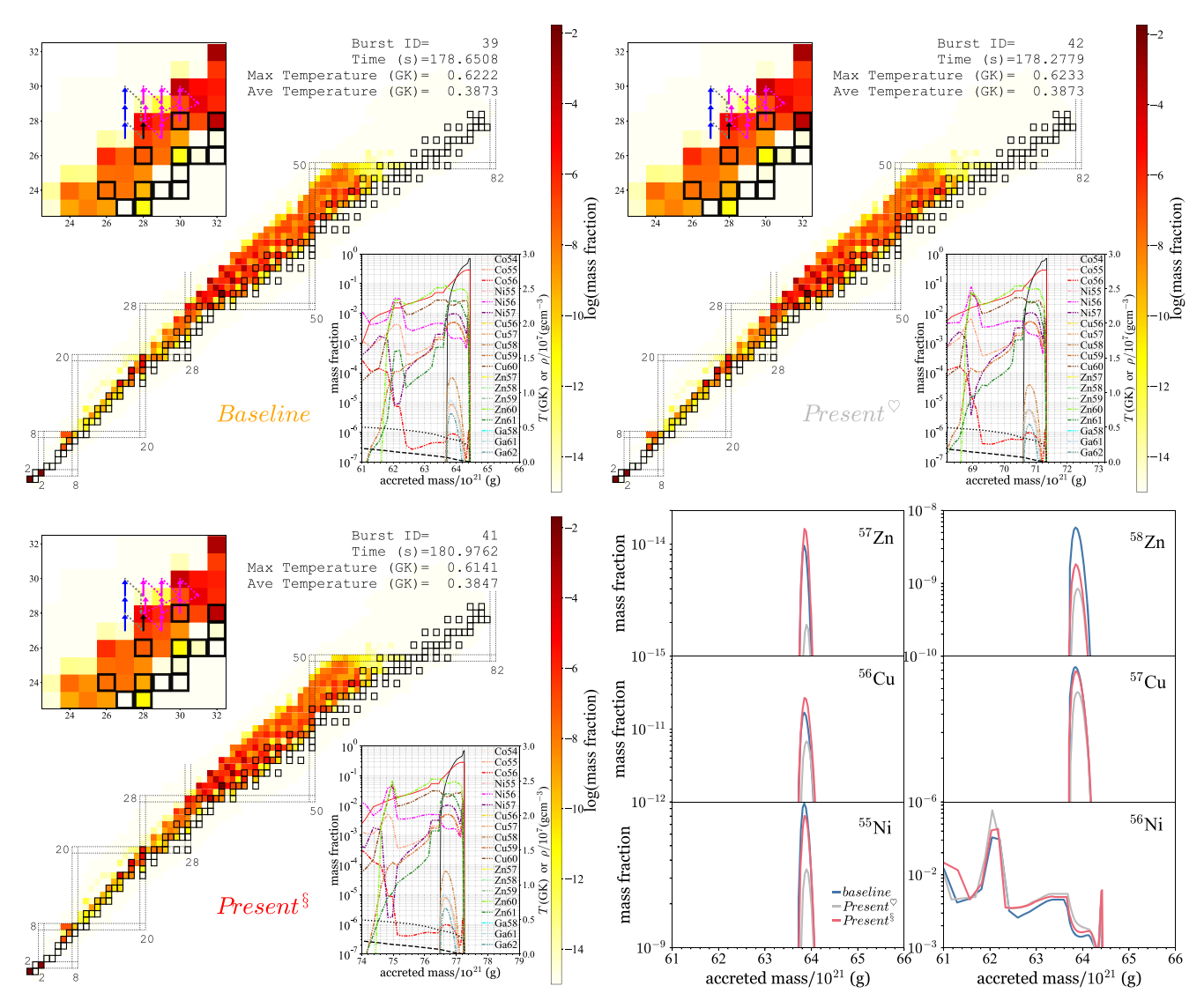


Figure 9. The nucleosynthesis and evolution of the envelope corresponds to the moment of around 180 s after the burst peak for the *baseline* (top-left panel), *Present*[©] (top-right panel), and *Present*[®] (bottom-left panel) scenarios. See Figure 6 for further description.

Figure 9. Although the lower limit of the Langer et al. (2014) rate at 0.23 GK $\lesssim T \lesssim 0.82$ GK is used for the $Present^{\heartsuit}$ model, the $Present^{\heartsuit}$ model still produces a set of 55 Ni, 56 Cu, and 57 Zn abundances lower than the ones of the baseline and $Present^{\$}$ models. Also, both baseline and $Present^{\$}$ models produce similar 55 Ni, 56 Cu, and 57 Zn abundances. This indicates the cumulated impact that is generated from the difference of a factor of 2 in temperature regime T=0.8-2 GK between the Present and Langer et al. 57 Cu(p, γ) 58 Zn reaction rates. Meanwhile, the correlated influence on the syntheses of nuclei in the NiCu cycles is also manifested due to the $Present^{57}$ Cu(p, γ) 58 Zn, 59 Cu(p, α) 56 Ni, Kahl et al. 56 Ni(p, γ) 57 Cu, and Valverde et al. 55 Ni(p, γ) 56 Cu reaction rates since the onset at t=-10 s.

The compositions of burst ashes generated by these three models are presented in Figure 10. The cumulated impact from the regulated NiCu I, II, and sub-II cycles based on the *Present* and Langer et al. $^{57}\text{Cu}(p,\gamma)^{58}\text{Zn}$ reaction rates manifests on the abundances of burst ashes. Using the *Present* $^{57}\text{Cu}(p,\gamma)^{58}\text{Zn}$ reaction rate, the production of ^{12}C is reduced to a factor of 0.2, and thus the remnants from the hot CNO cycle, e.g., nuclei

A = 17 and 18 are affected up to about a factor of 0.5 and 2.5, respectively. The abundances of the daughters of SiP, SCl, and ArK cycles are reduced (increased) up to a factor of 0.7 (1.2). The total abundance of ⁵⁶Ni and its remnant is increased by up to a factor of 1.2 due to the correlated influence between the new 56 Ni(p, γ) 57 Cu, 57 Cu(p, γ) 58 Zn, and 55 Ni(p, γ) 56 Cu reaction rates. Meanwhile, the abundances of nuclei A = 64-104produced by Present[©] are closer to baseline than the ones produced by *Present*^{\infty}. Furthermore, the abundances of nuclei A = 105-140 are decreased by up to a factor of 0.2 (red dots in the bottom panel of Figure 10). Note that the Present 57 Cu(p, γ) 58 Zn reaction rate produces a different set of burst ash compositions deviating from the one generated by Langer et al. 57 Cu(p, γ) 58 Zn reaction rate, especially the burst ash composition of sd-shell nuclei from A = 20-34. Due to the Langer et al. 57 Cu(p, γ) 58 Zn reaction rate, the abundances of nuclei A = 65-84 are reduced by up to a factor of 0.9, and the abundances of nuclei A = 100-134 are somehow closer to baseline than the ones generated from the Present 57 Cu(p, γ) 58 Zn reaction rate.

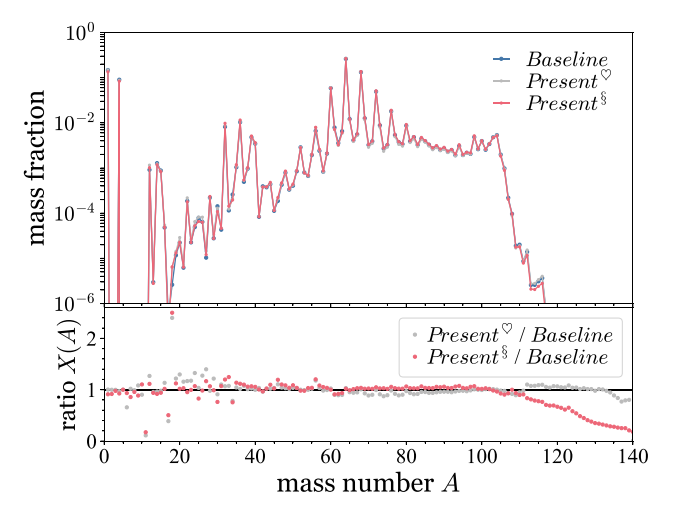


Figure 10. The averaged mass fractions for each mass number at burst tail when $t \approx 180 \text{ s}$.

The noticeable difference in the burst ash compositions from the *Present* and from Langer et al. $^{57}\text{Cu}(p,\gamma)^{58}\text{Zn}$ reaction rates exhibits the sensitivity of the $^{57}\text{Cu}(p,\gamma)^{58}\text{Zn}$ reaction in influencing the burst ash composition that eventually affects the composition of the neutron-star crust. Therefore, the currently more constrained $^{57}\text{Cu}(p,\gamma)^{58}\text{Zn}$ coupled with the latest $^{56}\text{Ni}(p,\gamma)^{57}\text{Cu}$ and $^{55}\text{Ni}(p,\gamma)^{56}\text{Cu}$ reaction rates constricts the burst ash composition, which is the initial input for studying superbursts (Gupta et al. 2007).

5. Summary and Conclusion

A theoretical study of the ${}^{57}\text{Cu}(p,\gamma){}^{58}\text{Zn}$ reaction rate is performed based on the large-scale shell-model calculations in the full pf-model space using GXPF1a and its charge-dependent version, cdGX1A, interactions. We present a detailed analysis of the energy spectrum of ⁵⁸Zn on the basis of the IMME concept with the aim to determine the order of l_1^+ and 2_3^+ states of ^{58}Zn that are dominant in the $^{57}Cu(p,\gamma)^{58}Zn$ reaction rate at T = 0.3-0.8 GK. As no firm assignment can be done due to the lack of experimental information on the ⁵⁸Cu spectrum, we test an alternative assignment to the previously adopted one. We have also estimated the energy of the 1^+_2 state of 58 Zn based on the currently available candidate for the isobaric analog states of ⁵⁸Cu and ⁵⁸Ni, which were experimentally determined, and the theoretical IMME c coefficient. We estimate the 1_2^+ state of $^{58}\mathrm{Zn}$ to be higher than the one predicted by the isospin-conserving interaction pf-shell interaction, GXPF1a. The dominance of the 1_2^+ state in the 57 Cu(p, γ) 58 Zn reaction rate at T = 0.8-2 GK is exponentially reduced. Throughout the course of a clocked burst, more than 60% of the mass zones in the accreted envelope is heated to T = 0.8-1.6 GK. The clocked XRBs of the GS 1826 -24 burster is more sensitive to the 57 Cu(p, γ) 58 Zn reaction rate at the temperature range $0.8 \lesssim T$ (GK) $\lesssim 1.6$ GK. Thus, the resonance energy of the dominant 1_2^+ state determining the 57 Cu(p, γ) 58 Zn reaction rate at T = 0.8 - 1.6 GK is important in influencing the extent of synthesized nuclei during clocked bursts of the GS 1826-24 burster.

Using the newly deduced 57 Cu(p, γ) 58 Zn, the newly corrected 55 Ni(p, γ) 56 Cu, and the updated 56 Ni(p, γ) 57 Cu reaction rates, we find that five combinations of these three reactions yield a set of light-curve profiles similar to the one generated by the *baseline* model based on the Forstner et al. (2001) and

Fisker et al. (2001) reaction rates which are labeled as *wien*2 and *nfis*, respectively, in JINA REACLIB v2.2. Nevertheless, the correlated influence on the nucleosyntheses shows that the 57 Cu(p, γ) 58 Zn reaction is critical in characterizing the burst ash composition. Constraining the 57 Cu(p, γ) 58 Zn reaction rate to be a factor of 5 lower than the *wien*2 rate and to be a factor of 2 lower than the Langer et al. (2014) rate at the temperature regime relevant for XRBs is important for us to have a more constrained initial neutron-star crust composition. We remark that the observed burst-tail end of Epoch Jun 1998 of the GS 1826–24 burster is closely reproduced by all models of the present work with the slightly adjusted astrophysical parameters.

Furthermore, we find that the redistribution and reassembling of reaction flows in the NiCu cycles also diminish the impact of 55 Ni(p, γ) 56 Cu reaction; though this bypassing reaction partially diverts material from the 56 Ni waiting point, the reaction flow eventually joins with the NiCu cycles and leaks out to the ZnGa cycles. Indeed, as indicated by the one-dimensional multizone hydrodynamic XRB model matching with the GS 1826-24 clocked burster, implementing the nfis 55 Ni(p, γ) 56 Cu reaction rate has already manifested the bypassing reaction flow of the 56 Ni waiting point without the implementation of the Valverde et al. (2019) 35 Ni(p, γ) 56 Cu reaction rate.

In addition, we notice that the weak GeAs cycle involving the two-proton sequential capture on ^{64}Ge , following the $^{64}\text{Ge}(p,\gamma)^{65}\text{As}(p,\gamma)^{66}\text{Se}$ branch, may exist shortly around the middle of onset until after the burst peak. The period of this transient existence may depend on the precise determination of the $S_{\rm p}(^{66}\text{Se})$ value. The *Present* $^{57}\text{Cu}(p,\gamma)^{58}\text{Zn}$ reaction rate, which is more constrained than Langer et al. (2014) reaction rate, was used by Lam et al. (2022) to study the weak GeAs cycles and was also recently used by Hu et al. (2021) to study the prevailing influence of the newly deduced $^{22}\text{Mg}(\alpha,p)^{25}\text{Al}$.

We are very grateful to N. Shimizu for suggestions in tuning the KSHELL code at the PHYS T3 (Institute of Physics) and QDR4 clusters (Academia Sinica Grid-computing Centre) of Academia Sinica, Taiwan; to D. Kahl for checking and implementing the newly updated 56 Ni(p, γ) 57 Cu reaction rate; to B. Blank for implementing the IMME framework; to M. Smith for using the Computational Infrastructure for Nuclear Astrophysics; to B. A. Brown for using the NUSHELLX@MSU code; and to J. J. He for fruitful discussion. This work was financially supported by the Strategic Priority Research Program of Chinese Academy of Sciences (CAS, grant Nos. XDB34000000 and XDB34020204) and the National Natural Science Foundation of China (No. 11775277). We are appreciative of the computing resource provided by the Institute of Physics (PHYS_T3 cluster) and the ASGC (Academia Sinica Grid-computing Center) Distributed Cloud resources (QDR4 cluster) of Academia Sinica, Taiwan. Part of the numerical calculations were performed at the Gansu Advanced Computing Center. Y.H.L. gratefully acknowledges the financial supports from the Chinese Academy of Sciences President's International Fellowship Initiative 2019FYM0002) and appreciates the laptop (Dell M4800) partially sponsored by Pin-Kok Lam and Fong-Har Tang during the COVID-19 pandemic. A.H. is supported by the Australian Research Council Centre of Excellence for Gravitational Wave Discovery (OzGrav, No. CE170100004) and for All Sky Astrophysics in 3 Dimensions (ASTRO 3D, No.

CE170100013). N.A.S. is supported by the IN2P3/CNRS, France, Master Project—"Exotic nuclei, fundamental interactions and astrophysics". A.H., A.M.J., and Z.J. were supported, in part, by the National Science Foundation under grant No. PHY-1430152 (JINA Center for the Evolution of the Elements, JINA-CEE).

ORCID iDs

Yi Hua Lam (藍乙華) forcid.org/0000-0001-6646-0745 Ning Lu (盧寧) forcid.org/0000-0002-3445-0451 Alexander Heger https://orcid.org/0000-0002-3684-1325 Adam Michael Jacobs https://orcid.org/0000-0002-3580-2420 Nadezda A. Smirnova https://orcid.org/0000-0001-

8944-7631

Teresa Kurtukian Nieto https://orcid.org/0000-0002-0028-0220

Zac Johnston https://orcid.org/0000-0003-4023-4488 Shigeru Kubono (久保野茂) https://orcid.org/0000-0003-0783-5978

References

```
Angulo, C., Arnould, M., Rayet, M., et al. 1999, NuPhA, 656, 3
Audi, G., Kondev, F. G., Wang, M., et al. 2017, ChPhC, 41, 030001
Brown, B. A., & Rae, W. D. M. 2014, NDS, 120, 115
Brussaard, P. J., & Glaudemans, P. W. M. 1977, Shell Model Applications in
  Nuclear Spectroscopy (North-Holland: Amsterdam)
Cyburt, R. H., Amthor, A. M., Ferguson, R., et al. 2010, ApJS, 189, 240
Cyburt, R. H., Amthor, A. M., Heger, A., et al. 2016, ApJ, 830, 55
Fisker, J. L., Barnard, V., Görres, J., et al. 2001, ADNDT, 79, 241
Forstner, O., Herndl, H., Oberhummer, H., Schatz, H., & Brown, B. A. 2001,
   PhRvC, 64, 045801
Fowler, W. A., Caughlan, G. R., & Zimmerman, B. A. 1967, ARA&A, 5, 525
Fowler, W. A., & Hoyle, F. 1964, ApJS, 9, 201
Fu, C. Y., Zhang, Y. H., Wang, M., et al. 2020, PhRvC, 102, 054311
Fujimoto, M. Y. 1988, ApJ, 324, 995
Fujita, H., Fujita, Y., Adachi, T., et al. 2007, PhRvC, 75, 034310
Fujita, Y., Fujita, H., Adachi, T., et al. 2002, EPJA, 13, 411
Galloway, D. K., Cumming, A., Kuulkers, E., et al. 2004, ApJ, 601, 466
Galloway, D. K., Goodwin, A. J., & Keek, L. 2017, PASA, 34, e019
Galloway, D. K., in' t Zand, J. J. M., Chenevez, J., et al. 2020, ApJS, 249, 32
Galloway, D. K., Muno, M. P., Hartman, J. M., et al. 2008, ApJS, 179, 360
Goodwin, A. J., Heger, A., & Galloway, D. K. 2019, ApJ, 870, 64
Gupta, S., Brown, E. F., Schatz, H., Möller, P., & Kratz, K.-L. 2007, ApJ,
   662, 1188
He, C.-C., & Keek, L. 2016, ApJ, 819, 47
Heger, A., Cumming, A., Galloway, D. K., & Woosley, S. E. 2007, ApJL,
  671, L141
Heger, A., Langer, N., & Woosley, S. E. 2000, ApJ, 528, 368
Herndl, H., Görres, J., Wiescher, M., & Wormer, L. V. 1995, PhRvC, 52, 1078
Honkanen, J., Kortelahti, M., Eskola, K., & Vierinen, K. 1981, NuPhA,
   366, 109
Honma, M., Otsuka, T., Brown, B. A., & Mizusaki, T. 2004, PhRvC, 69,
Honma, M., Otsuka, T., Brown, B. A., & Mizusaki, T. 2005, EPJAS, 25, 499
```

Horoi, M., Stoica, S., & Brown, B. A. 2007, PhRvC, 75, 034303

Iliadis, C. 2007, Nuclear Physics of Stars (Weinheim: Wiley)

talk), https://burst.sci.monash.edu/bern18/

Hu, J., Yamaguchi, H., Lam, Y. H., et al. 2021, PhRvL, 127, 172701

Jacobs, A. M., Heger, A., Johnston, Z., et al. 2018, in Burst Environment,

Reactions and Numerical Modelling Workshop (BERN18) (contribution

```
Johansson, E. K., Rudolph, D., Ragnarsson, I., et al. 2009, PhRvC, 80, 014321
Johnston, Z., Heger, A., & Galloway, D. K. 2020, MNRAS, 494, 4576
Jongsma, H., Silva, A. D., Bron, J., & Verheul, H. 1972, NuPhA, 179, 554
Joss, P. C. 1977, Natur, 270, 310
Joss, P. C. 1978, ApJL, 225, L123
Kahl, D., Woods, P. J., Poxon-Pearson, T., et al. 2019, PhLB, 797, 134803
Keek, L., & Heger, A. 2011, ApJ, 743, 189
Lam, Y. H., Blank, B., Smirnova, N. A., Bernard Bueb, J., & Susai Antony, M.
   2013b, ADNDT, 99, 680
Lam, Y. H., He, J. J., Parikh, A., et al. 2016, ApJ, 818, 78
Lam, Y. H., Liu, Z. X., Heger, A., et al. 2022, ApJ, 929, 72
Lam, Y. H., Smirnova, N. A., & Caurier, E. 2013a, PhRvC, 87, 054304
Langer, C., Montes, F., Aprahamian, A., et al. 2014, PhRvL, 113, 032502
Ma, S., Zhang, L., & Hu, J. 2019, Nucl. Sci. Tech., 30, 141
Makino, F. 1988, IAU Circ., 4653, 2
Meisel, Z., Deibel, A., Keek, L., Shternin, P., & Elfritz, J. 2018, JPhG, 45,
   093001
Möller, P., Nix, J. R., Myers, W. D., & Swiatecki, W. J. 1995, ADNDT,
   59, 185
Nesaraja, C. D., Geraedts, S. D., & Singh, B. 2010, NDS, 111, 897
Ong, W.-J., Langer, C., Montes, F., et al. 2017, PhRvC, 95, 055806
Ormand, W. E., & Brown, B. A. 1989, NuPhA, 491, 1
Ormand, W. E., & Brown, B. A. 1995, PhRvC, 52, 2455
Pearson, J. M., Nayak, R. C., & Goriely, S. 1996, PhLB, 387, 455
Poves, A., Sánchez-Solano, J., Caurier, E., & Nowacki, F. 2001, NuPhA,
  694, 157
Rauscher, T., & Thielemann, F.-K. 2000, ADNDT, 75, 1
Richter, W. A., & Brown, B. A. 2012, PhRvC, 85, 045806
Richter, W. A., & Brown, B. A. 2013, PhRvC, 87, 065803
Richter, W. A., Brown, B. A., Signoracci, A., & Wiescher, M. 2011, PhRvC,
   83, 065803
Rolfs, C. E., & Rodney, W. S. 1988, Cauldrons in the Cosmos (Chicago, IL:
   Univ. Chicago Press)
Rudolph, D., Andreoiu, C., Fahlander, C., et al. 2002, PhRvL, 89, 022501
Rudolph, D., Baktash, C., Dobaczewski, J., et al. 1998, PhRvL, 80, 3018
Rudolph, D., Fahlander, C., Algora, A., et al. 2000, PhRvC, 63, 021301
Rudolph, H., & McGrath, R. L. 1973, PhRvC, 8, 247
Schatz, H., Aprahamian, A., Barnard, V., et al. 2001, PhRvL, 86, 3471
Schatz, H., Aprahamian, A., Görres, J., et al. 1998, PhR, 294, 167
Schatz, H., Bertulani, C. A., Brown, B. A., et al. 2005, PhRvC, 72, 065804
Schatz, H., & Ong, W.-J. 2017, ApJ, 844, 139
Seth, K. K., Iversen, S., Kaletka, M., et al. 1986, PhLB, 173, 397
Shimizu, N., Mizusaki, T., Utsuno, Y., & Tsunoda, Y. 2019, CoPhC,
   244, 372
Smirnova, N. A., Blank, B., Brown, B. A., et al. 2016, PhRvC, 93, 044305
Smirnova, N. A., Blank, B., Brown, B. A., et al. 2017, PhRvC, 95, 054301
Steiner, A. W., Lattimer, J. M., & Brown, E. F. 2010, ApJ, 722, 33
Surbrook, J., MacCormick, M., Bollen, G., et al. 2019, HyInt, 240, 65
Tanaka, Y. 1989, in Proc. XXIII ESLAB Symp. on Two Topics in X-Ray
   Astronomy, ed. J. Hunt & B. Battrick (Noordwijk: ESA), 3
Ubertini, P., Bazzano, A., Cocchi, M., et al. 1999, ApJ, 514, L27
Valverde, A. A., Brodeur, M., Bollen, G., et al. 2018, PhRvL, 120, 032701
Valverde, A. A., Brodeur, M., Bollen, G., et al. 2019, PhRvL, 123, 239905
Van Wormer, L., Görres, J., Iliadis, C., Wiescher, M., & Thielemann, F.-K.
   1994, ApJ, 432, 326
Wallace, R. K., & Woosley, S. E. 1981, ApJS, 45, 389
Weaver, T. A., Zimmerman, G. B., & Woosley, S. E. 1978, ApJ, 225, 1021
Wiescher, M., Harms, V., Gorres, J., et al. 1987, ApJ, 316, 162
Wigner, E. P. 1957, Proc. Robert A. Welch Foundation Conf.: Benchmark
   Papers in Nuclear Physics 1, Nuclear Analogue States, ed. D. Robson &
   J. D. Fox, (New York: Wiley), 67
Woosley, S. E., Heger, A., Cumming, A., et al. 2004, ApJS, 151, 75
Woosley, S. E., & Taam, R. E. 1976, Natur, 263, 101
Woosley, S. E., & Weaver, T. A. 1984, in AIP Conf. Proc. 115, High Energy
   Transients in Astrophysics, ed. S. E. Woosley (New York: AIP), 273
```

Zhang, Y. H., Zhang, P., Zhou, X. H., et al. 2018, PhRvC, 98, 014319